Physics   College of Arts and Sciences

7-26-2005

The Cleo Rich Detector

Raymond Mountain
Syracuse University

Marina Artuso
Department of Physics, Syracuse University, Syracuse, NY

R. Ayad
Syracuse University

Konstantin Vladimirovich Bukin
Syracuse University

Recommended Citation

THE CLEO RICH DETECTOR

M. Artuso [a], R. Ayad [a], K. Bukin [a], A. Efimov [a],
C. Boulahouache [a], E. Dambasuren [a], S. Kopp [a], Ji Li [a],
G. Majumder [a], N. Menaa [a], R. Mountain [a], S. Schuh [a],
T. Skwarnicki [a], S. Stone [a,*], G. Viehhauser [a], J.C. Wang [a]

[a] *Department of Physics, Syracuse University, Syracuse, NY 13244-1130, USA*

T.E. Coan [b], V. Fadeyev [b], Y. Maravin [b], I. Volobouev [b], J. Ye [b]

[b] *Department of Physics, Southern Methodist University, Dallas, TX 75275-0175, USA*

S. Anderson [c], Y. Kubota [c], A. Smith [c]

[c] *School of Physics and Astronomy, University of Minnesota, Minneapolis, MN 55455-0112, USA*

Abstract

We describe the design, construction and performance of a Ring Imaging Cherenkov Detector (RICH) constructed to identify charged particles in the CLEO experiment. Cherenkov radiation occurs in LiF crystals, both planar and ones with a novel "sawtooth"-shaped exit surface. Photons in the wavelength interval 135–165 nm are detected using multi-wire chambers filled with a mixture of methane gas and triethylamine vapor. Excellent π/K separation is demonstrated.

Key words: Cherenkov, Particle-identification
PACS: 03.30+p, 07.85YK

* Corresponding author.
  Email address: stone@physics.syr.edu (S. Stone).

arXiv:physics/0506132v2 [physics.ins-det] 26 Jul 2005

1 INTRODUCTION

The CLEO II detector was revolutionary in that it was the first to couple a large magnetic tracking volume with a precision crystal electromagnetic calorimeter capable of measuring photons down to the tens of MeV level [1]. CLEO II produced many ground-breaking physics results, but was hampered by its limited charged-hadron identification capabilities that were provided by a combination of dE/dx and time-of-flight measurements.

The CLEO III detector was designed to study decays of b and c quarks, τ leptons and Υ mesons produced in e^+e^- collisions near 10 GeV center-of-mass energy. CLEO III is an upgraded version of CLEO II, as the magnet, the calorimeter and the muon system were kept. It contained a new four-layer silicon strip vertex detector, a new wire drift chamber and a particle identification system based on Cherenkov ring imaging described herein. Information about CLEO is available elsewhere [2,3].

Design choices for particle identification were limited by radial space and the necessity of minimizing material in front of the CsI crystal calorimeter. The CsI imposed a hard radial outer limit, and the desire for maintaining excellent charged particle tracking imposed a radial lower limit, since at high momentum the error in momentum is inversely proportional to the square of the track length. The particle identification system was allocated only 20 cm of radial space, and this limited the technology choices. To retain the superior performance of the calorimeter, a material thickness of only 12% of a radiation length was allowed.

The CLEO III installation including the RICH detector occurred in the summer of 1999 and was used to study physics in the e^+e^- center-of-mass energy region around 9-12 GeV. The two-ring machines KEKB and PEP-II produced much more luminosity than CESR, and after some excellent initial results on B decays and Upsilon spectroscopy, it became clear that there was much physics to be explored in charm decays and studies of charmonium. The transformation from CLEO III to CLEO-c was made in 2003, when the CESR accelerator began operating in the 3-5 GeV center-of-mass energy region. The inner double-sided silicon detector was replaced with a wire drift chamber that has significantly less material and is much better suited to the CLEO-c physics program; in any case, the silicon was showing effects of premature radiation damage. The magnetic field was lowered from 1.5 T to 1 T, mainly for accelerator related considerations.

The plan of this paper is as follows: The basic RICH detector design will be delineated, followed by descriptions of the individual components, namely the crystals, multi-wire chambers, superstructure, readout electronics, and

support subsystems. Issues in the long-term operation of the RICH are then discussed. Finally, some details of the data analysis technique and physics performance are presented.

2 DETECTOR OVERVIEW

2.1 Design Choices

The severe radial spatial constraint forces the design to have a thin, few-cm detector for Cherenkov photons and a thin radiator. Otherwise the photons have too little distance to travel and it becomes very difficult to precisely measure the photon angles. In fact, the only thin, large-area photon detectors possible in our situation were wire chamber based, either using a reflective CsI photocathode or a gas mixture of methane (CH_4) and triethylamine (TEA) vapor to convert ultraviolet photons.[1] Use of CsI would have allowed us to use a liquid freon radiator with quartz windows in the system and to work in the wavelength region from about 160–200 nm. However, at the time of decision, the use of CsI was far from proven and, in any case, would have imposed severe constraints on the construction process, which would have been both technically difficult and expensive. Thus we chose a multi-wire chamber filled with a mixture of CH_4 and TEA that uses Cherenkov photons in the vacuum ultraviolet (VUV) region, 135–165 nm, generated in a 1 cm thick LiF crystal.

The quantum efficiency of the CH_4 and TEA mixture peaks at ∼150 nm [4], as shown in Fig. 1, below the transmission cutoff for glasses and fused silica quartz. This short wavelength requires the use of alkali halide crystals as both the Cherenkov-emitting medium and the entrance window to the photosensitive volume [5]. We chose LiF as the Cherenkov radiator because it has the lowest dispersion in the wavelength band of the CH_4-TEA quantum efficiency [6]. Transparent gases must be used between the radiator and the photon detector that are almost entirely free of O_2 and H_2O, both of which have 1–10 Mbarn cross section for photon absorption below 175 nm [7].

Details of the design of the CLEO RICH have been discussed elsewhere [8,9]. Here we briefly review the main elements. Cherenkov photons are produced in a LiF radiator. The photons then traverse a free space, an "expansion volume," where the cone of Cherenkov light expands in size. The photons enter a detector consisting of spatially-segmented multi-wire chambers (MWC) filled with CH_4 gas mixed with TEA vapor, in which they are converted to

---

[1] A TMAE-based photon detector would have been unacceptably thick in order to obtain the same detection efficiency, due to its long photon absorption length.
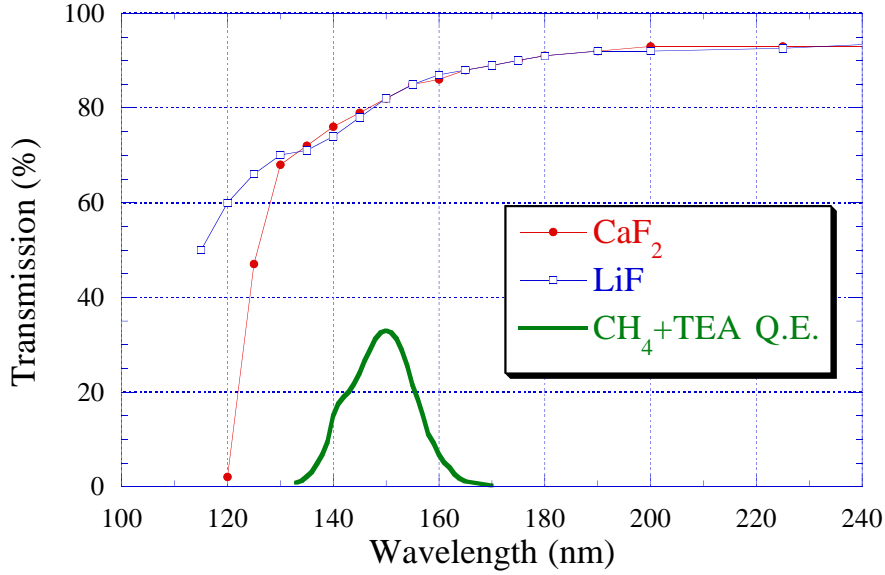
Fig. 1. The transmission of the LiF and CaF$_2$ optics for the CLEO RICH, along with the measured quantum efficiency of CH$_4$ plus TEA gas [4].

electrons and multiplied. Finally, signals are picked up with sensitive low-noise electronics. No optical focusing elements are used; this is called "proximity-focusing" [6]. The scheme is shown in the upper left of Fig. 2, while the placement in CLEO is shown in Fig. 3.
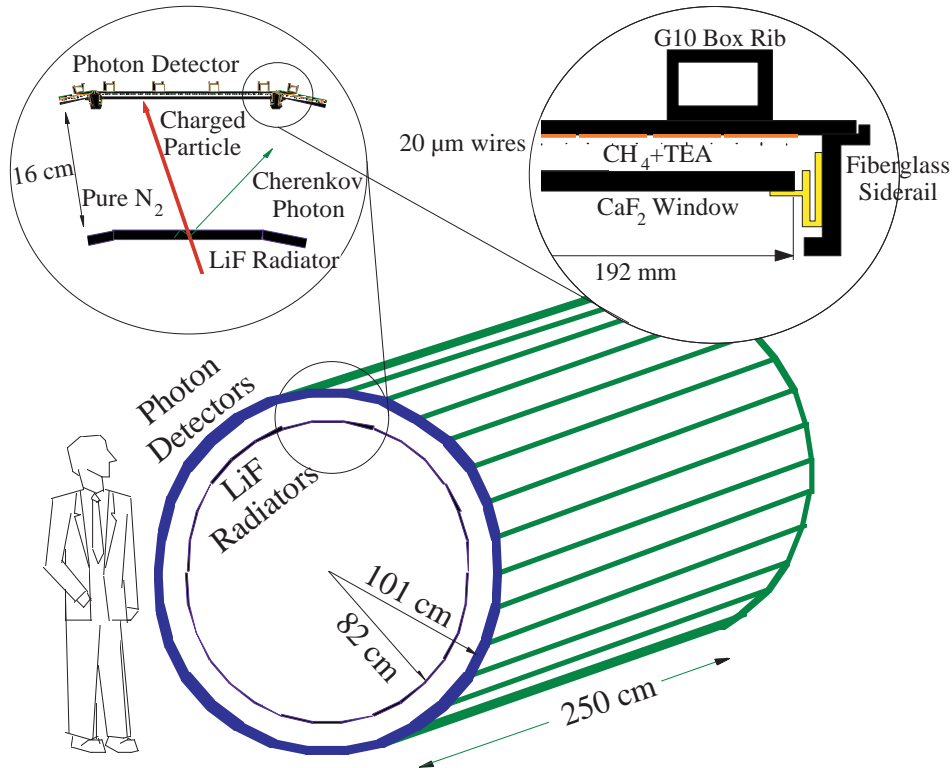

Fig. 2. Outline of the CLEO RICH detector design.

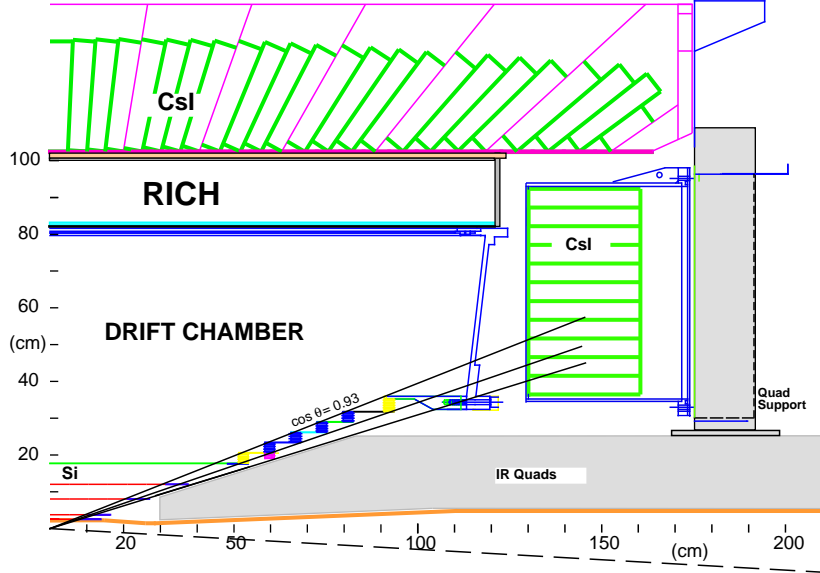There are 30 individual photon detectors around the outer cylinder. They

Fig. 3. The CLEO RICH, shown in CLEO-III configuration.

subtend the same azimuthal angle as the radiators, which are segmented into 30 rows and 14 rings on the inner cylinder. The expansion volume between the radiators and detectors is filled with pure N_2 gas. In fact, any transparent, pure gas could be used. Our choice was based on the availability of very pure gas from the super-conducting coil boil off.

The most distinctive features of the design of the CLEO RICH are: (1) ultra-thin photon detectors, with high spatial segmentation and almost full area coverage; (2) a large volume of high-purity, VUV-transparent crystals including a novel "sawtooth" geometry; and (3) exceptionally low-noise analog electronics readout.

2.2   Radiators

LiF was chosen over CaF_2 or MgF_2, both of which are transparent in the VUV wavelength region, due to its lower dispersion leading to smaller chromatic error. Originally all the radiators were planned to be 1 cm thick planar pieces. However, since the refractive index of LiF at 150 nm is 1.5, all the Cherenkov light generated from tracks normal to the LiF surface would be totally internally reflected, as shown in Fig. 4 (top). We could have used these planar radiators, but we would have had to tilt them at about a 15° angle. Besides the obvious mechanical support problem, some tracks would produce Cherenkov photons that would cross through the entire thickness of another radiator tile causing a loss of efficiency and reconstruction problems. Instead, we developed novel radiators with a serrated top surface, called "sawtooth" radiators [10], as shown in Fig. 4 (bottom). Measured physical properties of

5

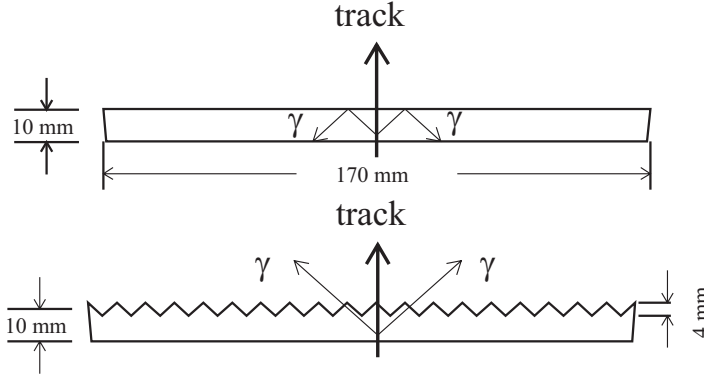the radiators have been described previously [8].

Fig. 4. Sketch of a plane radiator (top) and a sawtooth radiator (bottom). Cherenkov light paths radiated from a charged track normal to each radiator are shown.

The overall radiator shape approximates a cylinder of radius 82 cm. Individual radiator crystals are placed in 14 coaxial rings of 30 crystals each, centered around the beam line and symmetrically positioned about the interaction point. The 30 crystals segments are parallel to the wire chambers. Inter-crystal gaps are typically 50–100 μm. The crystals are attached to the exterior surface of a 1.5 mm thick carbon fiber shell with a low outgassing epoxy.

The inner four rings are made of sawtooth radiators. Lengthy production time as well as cost limited our use of these novel objects.

2.3 Photon Detectors

The photon detectors have segmented cathode pads 7.5 mm (length) × 8.0 mm (width) etched onto G10 printed-circuit boards (PCBs). The pad array was formed from four individual boards, each with 24 × 80 pads, the latter split into two 24 × 40 pad sections with a 7 mm gap. Each board was individually flattened in an oven and then they were glued together longitudinally on a granite table where reinforcing G10 ribs were also glued on. The ribs have a box-like structure. There are 4 longitudinal ribs that traverse the entire length. Smaller cross ribs are placed every 12 cm for extra stiffening. The total length of the pad array is 2.46 m.

Wire planes were strung with 20 μm diameter gold plated tungsten with a 3% admixture of rhenium; the wire pitch was 2.66 mm, for a total of 72 wires per chamber. The wires were placed on and subsequently glued to precision ceramic spacers every 30 cm. The spacers extend 1 mm above the cathodes, and therefore are 3.5 mm from the CaF$_2$ windows. We achieved a tolerance

of 50 μm on the wire to cathode distance. The spacers had slots in the center for the glue bead.

Eight 30 cm × 19 cm CaF$_2$ windows were glued together in precision jigs lengthwise to form a 2.4 m long window. Positive high voltage is applied to the anode wires, while negative high voltage is put on 100 μm wide silver traces deposited on the CaF$_2$. The spacing between the traces is 2.5 mm, and they are connected together by a trace running across both edges. The pad plane is close to ground. The gain of the chamber depends on the amount of high voltage on wires and windows. We define "wire-gain," in the normal manner, as the multiplication factor on a single electron. We run the system at typical wire-gains around 30,000. "Pad-gain" is our usual measure of multiplication and is calculated as being 75% of the wire-gain.

To maintain the ability of disconnecting any faulty part of a chamber, the high voltage is distributed independently to three groups of 24 wires and the windows are each powered separately.

2.4 Electronics

The position of Cherenkov photons is measured by sensing the induced avalanche charge on the cathode pad array. Since the pulse height distribution from single photons is expected to be exponential at low to moderate gas gains [11], the use of low noise electronics is required to ensure high detection efficiency. Pad clusters in the detector can be formed from single Cherenkov photons, overlaps of more than one Cherenkov photon, or charged tracks. In Fig. 5 we show the pulse height distribution for single photons and charged tracks. (Note, one ADC count corresponds to $\sim$200 electrons.) These can be separated by just examining the pulse height. The charged tracks give very large pulse heights because they are traversing $\sim$4.5 mm of the CH$_4$-TEA mixture. We can distinguish somewhat between the charge due to single photons and two photons because of the pulse height shapes on adjacent pads.

To have as low noise electronics as possible, a dedicated VLSI chip, called VA_RICH, based on a very successful chip developed for solid state applications, has been designed and produced for our application at IDE AS, Norway [13]. We have fully characterized 3,600 64-channel chips, mounted on hybrid circuit boards. For moderate values of the input capacitance C_{in}, the equivalent noise charge measured ENC is found to be about

$$ENC = 130\,e^- + (9\,e^-/\text{pF}) \cdot C_{in} \quad . \tag{1}$$

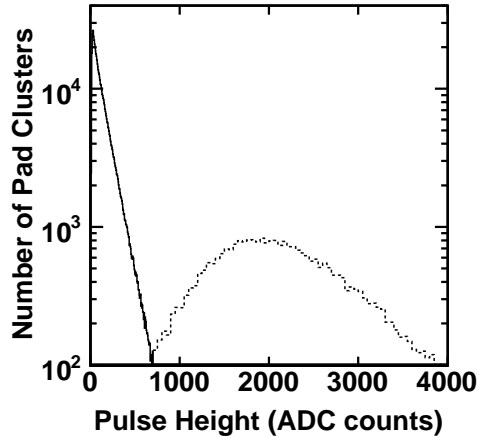The dynamic range of the chip is between 450,000 and 900,000 electrons,

Fig. 5. Pulse height distributions from pad clusters containing single photons (solid histogram) and charged tracks (dashed histogram). The photon data is consistent with an exponential distribution. One ADC count corresponds to ∼200 electrons. The charged track distribution is affected by electronic saturation.

depending upon whether we choose a bias point for the output buffer suitable for signals of positive or negative polarity or we shift this bias point to have the maximum dynamic range for signals of a single polarity.

In our readout scheme we group 10 chips in a single readout cell communicating with data boards located in VME crates just outside the detector cylinder. Chips in the same readout cell share the same cable, which routes control signals and bias voltages from the data boards and output signals to the data boards. Two VA_RICH chips are mounted using wire bonds on one hybrid circuit that is attached via two miniature connectors to the back of the cathode board of the photon detector.

The output of the VA_RICH is transmitted to the data boards as an analog differential current, transformed into a voltage by transimpedance amplifiers and digitized by a 12-bit differential ADC. These receivers are part of very complex data boards which perform several important analog and digital functions. Each board contains 15 digitization circuits and three analog power supply sections providing the voltages and currents to bias the chips, and calibration circuitry. The digital component of these boards contains a sparsification circuit, an event buffer, memory to store the pedestal values, and the interface to the VME crate CPU.

Coherent noise is present. We eliminate this by measuring the pulse heights on all the channels and performing an average of the non-struck channels before the data sparsification step. [2] The pedestal width (r.m.s.) is reduced from 3.6

---

[2] This algorithm is executed by a DSP located on the data boards before the data are sparsified.

to 2.5 ADC counts after this coherent noise subtraction. The intrinsic noise of the system then is $\sim$500 electrons r.m.s.

3   CRYSTAL FABRICATION and TESTING

The design of the CLEO RICH demands a large number of high-quality, high-purity VUV-transparent crystals, used as the entrance window to the multi-wire photon detectors and as the solid Cherenkov radiator medium. In fact, nearly 420 kg of crystal was required, in the form of 240 full-sized windows and 420 radiator tiles. The full windows were $191.0 \times 307.6 \times 2.0$ mm^3 in size, and the planar radiators were $174.3 \times 169.8 \times 10.0$ mm^3.

There were several significant issues in the production of these crystal pieces. First, the bulk absorption of VUV photons needed to be small, so high purity raw material was required. Second, the surface transmission needed to be appreciable, so high-quality polishing of the surfaces was required. These two elements are necessary to yield good transmission in the VUV region. Third, the finished plates needed to have large dimensions, so the active area of the detector remained high. Last, they needed to have good mechanical stability—free of cleaves, nascent cleaves, and geometric shape deformations—so the internal strain in the crystals needed to be minimal. This was particularly critical for the very thin 2 mm windows, which would cause the photon detector to fail if a crack occurred in situ. In order to meet these stringent requirements a R&D program in the areas of fluoride crystal growth and processing were undertaken.

3.1   Crystal Production

3.1.1   Crystal Growth Process

Fluoride crystals were grown at the Optovac facilities [14] using a modified Bridgman-Stockbarger method [15]. In this technique, pure raw powder is packed in a graphite crucible which is heated in a vacuum furnace to a temperature far above its melting point. After a period of impurity removal, the crucible is reduced to a temperature just above the melting point, and then slowly lowered mechanically through a sharp thermal gradient into a second volume where the temperature is below the melting point. This effects a surface of solidification in the melt where the crystal lattice is actually grown. The resulting solid ingot is then held at a reduced temperature (roughly half that of the melting point [16]), at which it is annealed to reduce the bulk strain induced by the growth process as it is slowly brought to room temperature.

The growth process is the most important single step in crystal production, since it not only impacts the manufacturability directly, but the ultimate optical and mechanical properties of the finished crystal as well. Stockbarger recognized from the beginning the critical roles of both the high purity of the raw material and the sharpness of the thermal gradient between the two temperature regions. This latter impacts the design and operation of the furnace, as does the need for uniformity of temperature in the melt. Good control of the crystallization zone allows for low intrinsic strain growth, and for the impurities to segregate to the top of the ingot. Both are necessary for the large-area RICH crystals.

The actual temperature levels and durations in the thermal cycle were determined by repeated experimentation, and varied according to material used and ingot size. This optimization constituted an important line of development, in particular for the large 14.5 and 16-inch diameter ingots grown for CaF_2 windows.[3] The CaF_2 ingots were grown using a piece of single crystal as a seed, in order to reduce the number of domain boundaries between regions of different crystal orientation. This was never entirely successful, and all ingots grown were polycrystals.

The raw material used was either very pure grade LiF powder synthesized by Merck,[4] or crushed natural fluorite (CaF_2), of sufficient purity for thin windows. In order to remove residual impurities from the fluorite, 2% PbO_2 was added as a getter that subsequently segregated from the melt. Any residual impurities reduce transmission significantly at 150 nm, since they will either create absorption (color) centers or scattering centers for light in the VUV region.

In order to monitor the ingot quality at growth, test bars were taken as a vertical slice from the periphery of each ingot. The transmission of these witness pieces from a representative early bad ingots containing relatively high impurity levels and good ingots produced after the growth process was optimized are shown in Fig. 6. This allowed the proofing of the ingots, as well as a diagnostic of growth problems.

3.1.2   Crystal Machining

The machining process consisted of taking a single ingot and producing many "blanks" from it—each of which is a formed piece of crystal ready for polishing in order to have good optical transmission. To produce the blanks, the ingot is first mounted on a plaster base and sliced to approximate thickness on a band-

---

[3] Large ingot growth also has important implications for other applications, such as 157 nm lithography for VLSI fabrication.
[4] LiF Optipur (R) powder, Merck SA, Darmstadt D-64293, Germany.
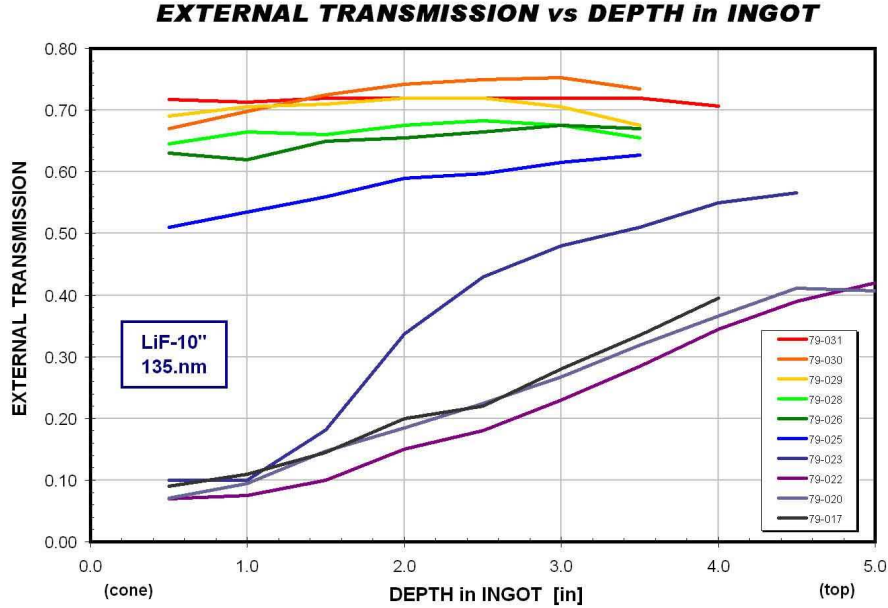
EXTERNAL TRANSMISSION vs DEPTH in INGOT

Fig. 6. Test bar transmission as a function of vertical position in the LiF ingot, at 135 nm, from 10 ingots grown in the same furnace. The low transmission curves show earlier bad growths having high levels of impurities (including Fe), while the high transmission curves come from later ingots, made after the growth process was optimized. The left end of the plot refers to the end of the ingot that is cone shaped, the bottom, while the right side shows the top.

saw using a diamond blade and a gravity-feed table. It is important to use a "well-cutting blade," [5] to thermalize the ingot and lubricant to room temperature, and to establish the proper feed rate of the blade through the ingot. Next, the slice is trimmed to approximate shape, and all edges are bevelled by hand. Then, the two faces of the slice are ground to within ~150 μm of final thickness, using a Blanchard-type surface grinder with fine-grit superabrasive pellets. Finally, the four edges of the piece are ground to dimension using a SX CNC machine with a very fine diamond superabrasive wheel. The LiF radiators have two edges which are given a 6° angle.

For the case of windows and planar radiators, the blank is now finished and ready for polishing. For the case of sawtooth radiators, additional grinding steps (as well as a different polishing technique) are required, as described below.

The machining process is developed by determining the proper speeds and feed rates for each operation. Otherwise the crystal may be easily destroyed.

---

[5] A "well-cutting" blade is not only sharp (e.g., using a diamond abrasive), but is properly dressed and lubricated so as to prevent loading up with fine crystal silt as it cuts. Thus the blade will cut the ingot instead of rubbing and cracking it. This same criteria is applied to the other cutting tools and grinding wheels used.

Fig. 7. Photograph of a polishing table, showing the lapping surface and rotating crystal carriers. Weights are placed on the crystals.

Nevertheless, each of these machining steps does introduce some actual damage to the crystal. This consists of microscopic cleaves and irregularities at the surface and just below it, called "subsurface damage." The goal of each step in the machining process is to cut away enough material so as to get under the subsurface damage created by the previous step, while itself creating at worst only a finer level of damage, which is to be removed by the subsequent operation. In this way, a piece of sufficient transmission is ultimately produced.

3.1.3 Crystal Polishing

The polishing process consisted of placing a blank on a lapping table with a polyurethane polishing pad and a specific polishing media, such as fine-grit diamond powder suspended in glycol or a commercially-available polishing slurry. Fig. 7 shows a working polishing table. The blank is weighted but free to spin within a rotating holder on the rotating polishing pad, the net effect of which is randomized orbits of the fine abrasive with respect to the blank. This yields a uniform action as it cuts away stock (mechanically or chemically) to get under the subsurface damage. This procedure is repeated with a finer grit abrasive, in order to finish the surface.

This is a fine and somewhat delicately balanced procedure, taking many hours per surface. The effectiveness is governed principally by the total amount of stock removed, which is related to the amount of weight applied to the piece as it glides on the polishing pad. The rate of stock removal also depends on the material (CaF_2 or LiF) and on the orientation of the crystal. The effectiveness

of different polishing times and weights was extensively studied.

3.1.4   Production Yields

Nearly one thousand individual crystals were produced for the CLEO RICH. The early stages of the crystal production saw a very low yield of pieces. It was only after intense efforts developing all phases of production (growth, machining and polishing) that the yields grew to acceptable levels.

For CaF_2 production, the intrinsic strain in the thin large-area windows needed to be minimized. Optimization of the annealing cycle, major improvements to the machining process, and determination of proper weighting during polishing, gave rise to increased yields. The manufacturing yield of an ingot (i.e., the number of windows produced divided by the number possible in an ingot) grew from below 30% in the initial phases of the project to be routinely above 80%, and as high as 90%. In the wake of these improvements, the quality of the ingot (i.e., the fraction of windows produced that passed CLEO requirements) also rose to be close to 100%.

For LiF production, proper purity of the material needed to be maintained. Improvements parallel to those made for CaF_2, as well as critical corrections to raw material handling, contributed to slowly increasing yields. For the first twenty LiF ingots grown, the manufacturing yield was under 40% with the quality about the same. Several episodes of material contamination then reduced the quality to effectively zero, as indicated in Fig. 6. This was due to insufficient segregation of impurities, or overabundance of impurities, both of which create color centers in the bulk material as well as enhanced domain boundaries. The latter creates "fault lines" along which the crystal may separate into multiple pieces, thereby becoming useless. As improvements were made during the second half of the project, the manufacturing yield grew to 70%, albeit with large fluctuations, due mainly to the continued presence of separating domain boundaries in some ingots. Also in later production, the quality of the ingots became quite high, far surpassing CLEO requirements even at 135 nm. This is also indicated in Fig. 6.

3.2   Crystals for Chamber Windows

There were 240 full-sized chamber window crystals required. A total of 300 were delivered, of which 272 were used in construction. To make the number of full-sized windows used, there were 393 individual crystals, of which 151 were full-sized CaF_2 crystals, 182 were half-sized CaF_2 crystals, and 60 were half-sized LiF window crystals. This small admixture of LiF windows
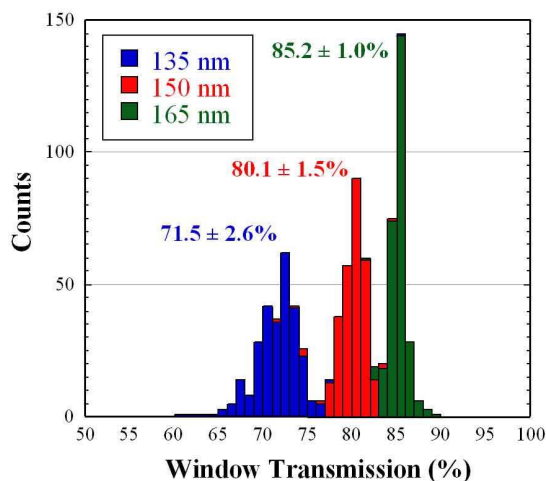
Fig. 8. Distribution of average window transmissions at 135, 150, and 165 nm, for all full size and half size CaF_2 and LiF windows.

was acceptable if the machining process succeeded, and sped up the chamber production schedule. An additional 16% were rejected for various reasons.

3.2.1 Inspection and Testing

All window crystals were cleaned, inspected and tested individually. Fig. 1 shows typical transmission curves for a 2 mm thick CaF_2 window and for a 10 mm thick LiF planar radiator. The main features on these curves are the drop to zero transmission at the band edge for the crystals (120 nm for CaF_2 and 105 nm for LiF). There are also several possible absorption lines at 130, 142.5, and 175 nm from water impurities. The transmission above 180 nm rises to more than 90% where bulk impurities cause minimal loss and only surface reflections dominate. For speed of processing of the crystals, most parts were scanned over their surface at 3 wavelengths only, namely 135, 150, and 165 nm, for each piece on a grid of 30 points over its surface, using the VUV Spectrophotometer system at Syracuse University, described in Appendix A.

Fig. 8 shows the distribution of transmissions at each of these wavelengths for all window crystals. Variations in the transmission may result from bulk impurities which vary by ingot, from polishing non-uniformities, and from variations in the cleaning. The variation at 135 nm are clearly larger than at 165 nm, and reflect the greater influences of water and other impurities below 145 nm. On average, the transmission in the windows is 71.5, 80.1, and 85.3% at 135, 150, and 165 nm, respectively, which matches our design criteria of 72, 80, and 85% at these wavelengths. All windows were tested both before and after high voltage trace deposition.
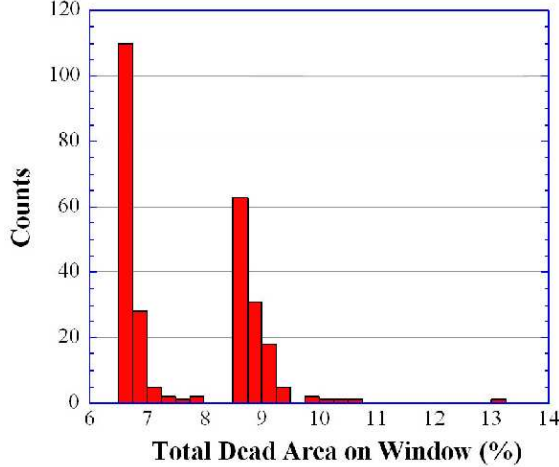
14

Fig. 9. Distribution of optically inactive area for CaF_2 and LiF windows. The two peaks correspond to windows made with full plates (left) and half plates (right).

The dominant mechanism for transmission loss was generally surface scattering or absorption, with bulk absorption accounting for <20% of the transmission loss. This was confirmed by transmission measurements of identically-prepared LiF and CaF_2 pieces of different thicknesses to separate the two effects.

On some crystals, cleaves were found to have propagated after production. In the case where the cleave was small and near an edge, the pieces were hand-worked to remove the cleave and get under the subsurface damage. If properly done, there was only a small probability that the cleave would reappear and propagate in a relevant amount of time. This was often successful and the best of these reworked pieces were used as chamber windows.

Fig. 9 shows the fraction of each window that was optically inactive. Factors which contribute to the inactive area include the window traces which typically contributed a 4% opacity, any mechanical defects such as missing corners, any reworked areas of cleave removal as mentioned above, or surface stains which were not easily cleaned with acetone. Additionally, due to production schedules and the detector installation deadline, the windows formed out of half-sized plates epoxied together in pairs had an extra glue joint resulting in an additional 2% loss of active surface area. The two peaks in Fig. 9 represent the whole and the half windows, with the tails in each distribution coming from defects, smudges, or coating problems.

3.2.2   Deposition of Traces

The CaF_2 crystals serve a dual role as entrance windows into the wire chambers, as well as high voltage cathodes for these chambers. In order to apply a voltage to this plane, a 200 nm thick coating of nickel and silver was applied

Fig. 10. The coating chamber for sputtering the metallized strips on the CaF$_2$ windows. In the foreground are the tungsten filaments which will vaporize the silver onto the crystals. The four crystals in the background lay behind steel masks with 100 μm slots cut into them to define the high voltage traces.

to the chamber side of the window. This coating was in the form of 100 μm wide strips spaced 2.54 mm apart, and connected at each of their ends by another metallized coating to act as a voltage distribution bus bar. During construction, a metal conductor was glued to this bus bar using conductive epoxy.

The metallized coating was performed by EMF;[6] the setup is shown in Fig. 10. The coating was a standard sputtering process, in which a stream of metal ions is created by placing loops of nickel or silver on tungsten filaments through which a 100 Amp current passes. The crystals and filaments are placed in a vacuum chamber for the sputtering process. The nickel was found to bond better to the CaF$_2$ surface, so a 50 nm layer of this was laid down first, followed by 150 nm layer of the silver. The strip features on the windows were defined by metal masks placed in contact with the windows which had 100 μm wide slots cut into them. These masks were held in contact with the crystal by placing the crystal on a machinist's magnetic chuck and pulling on the steel mask with the field from the chuck. Careful preparation of the chucks were required to make them vacuum-compatible and prevent outgassing onto the crystals. The masks were heat-treated to make them flat enough to not rise more than $\sim$ 25 μm off the crystals. If the mask was not held in intimate contact with the crystals, the sputtered silver would tend to "feather" under the mask, making a broad coated area that was then optically opaque.

---

[6] Evaporated Metal Films Corp., Ithaca, NY 14850.

3.3   Crystals for Radiators

There were 420 full-sized radiator crystals required, of which 300 were of planar and 120 were of sawtooth geometry. A total of 436 were delivered, from which 420 were used. To make the full radiator array, there were 450 individual crystals, of which 270 were full-sized LiF planar crystals, 60 were half-sized LiF planar crystals, and 120 were full-sized LiF sawtooth crystals. Pairs of half crystals were alternately used as the end rings to make the radiator left-right symmetric. An additional 2% of the planar radiators were rejected for various reasons, whereas for sawtooth radiators there were 23% rejected, indicating the relative difficulty in production.

3.3.1   Inspection and Testing

All radiator crystals were cleaned, inspected and tested individually. For planar radiators, the transmission was measured at 135 nm, 142 nm, 150 nm, and 165 nm, for each piece on a grid of $\sim$300 points over its surface, using the VUV Spectrophotometer system at SMU, described in Appendix A. On average, the transmission in the planar radiators is 65.5, 77.6, and 85.4% at 135, 150, and 165 nm, which matches our design criteria of 66, 77, and 85% at these wavelengths. However, the low value at 135 nm is misleading: it is an average which includes early ingots having low transmission due to an excess of impurities. Later ingots produced radiators with transmissions at 135 nm of up to 75%.

3.3.2   Dielectric Coating of Radiator Crystals

Monte Carlo studies indicated that the Cherenkov angle reconstruction efficiency is enhanced if those radiator photons entering the RICH photon detectors which have first bounced off the bottom surface of a radiator crystal are suppressed. Correspondingly, we coated the bottom surfaces of all 120 sawtooth radiator crystals with a thin layer of polystyrene. This dielectric has an index of refraction well matched to that of LiF. Detailed tests confirmed that this material strongly absorbs at 150 nm.

3.3.3   Techniques for Sawtooth Radiators

The unique geometry of the sawtooth radiator crystals cannot be accomplished using the fabrication methods described above. While the lower surface and edges of the sawtooth radiators are flat and may be polished using conventional orbital lapping techniques, special procedures were developed to produce high-quality VUV-polished faces in the "vee"-shaped grooves on the exit surface

of the crystals. These new techniques could, in principle, be adapted to other new geometries.

Sawtooth radiator blanks are cut and ground to a thickness of 12.7 mm (i.e., 0.7 mm oversized) in a manner identical to plane radiators. The blanks are then mounted on a linear surface grinder to define the groove shapes. A set of ten 6-inch diameter grinding wheels are mounted on a single spindle. These wheels are edged with a 90° "vee" on their edges and rough-grit superabrasive. Grooves are ground into the upper surface of each blank to within 1.0 mm of the final depth. Since there are 19 grooves in a sawtooth piece, this is done in two operations. Following this step, the group of ten wheels is replaced with a single grinding wheel with a 96° included angle and a fine-grit bond. This single wheel is then used to finish-grind the last $\sim$0.9 mm of depth in each of the grooves, thereby minimizing groove-to-groove differences within a single radiator crystal. As with the planar pieces, the fine-grit operation was found to reduce subsurface damage from the grinding process. The wheels need to be maintained by dressing periodically to remove LiF build-up, and to re-define the profile of the edge which rounds after grinding. Care was taken to reduce any spurious vibrations in the spindle during this procedure.

Polishing is done using a conventional Bridgeport milling machine with automated travel. Unlike the grinding, which could address both left and right faces of each groove simultaneously, the polishing is applied to one face of all grooves first and then applied to the remaining face in turn. The milling head is set at a 42° angle from the vertical and a new head is mounted in place of a milling bit. The polishing head was a 6-inch diameter aluminum disk with a soft polishing pad attached on the bottom, as is used on the usual lapping tables. The crystals are polished by applying a small tool pressure to the groove faces with this rotating head, and wetting the part with a polishing slurry. The part passes back and forth several times under the rotating head which reaches down into the groove. Then the part is indexed to work the next groove. After all grooves are done, the tool pressure is re-adjusted and a second set of passes taken. The piece is rotated in order to polish the opposite faces on the crystal. This entire procedure is repeated with a smaller grit abrasive, in order to finish the piece.

In order to test the optical transparency of the sawtooth radiators, we compared them to a calibrated prism of 42° inclination angle which was conventionally polished and also met our transmission specifications.[7] To compare a sawtooth radiator to the calibrated prism, we deflected the light incident on the flat face of the sawtooth or prism by 15° to avoid total internal reflection, and the light intensity through the sawtooth is compared to that of the prism.

---

[7] We fabricated two such prisms and measured the transmission of the two stacked together for a VUV beam incident at 15° angle to avoid total internal reflection.
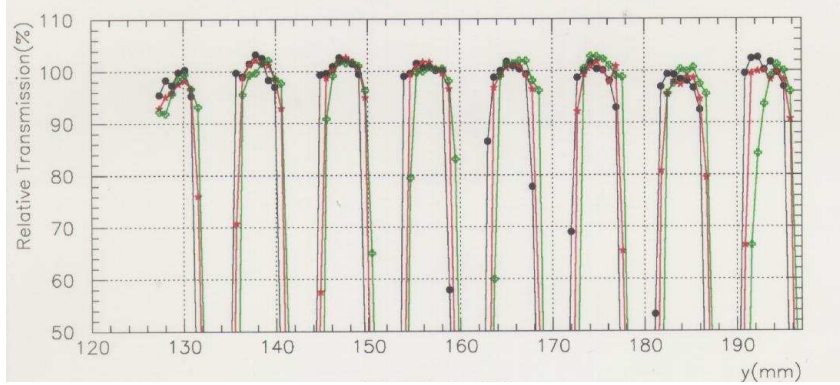
Fig. 11. Relative transmission scan over almost one-half of a typical sawtooth crystal, showing one face only. The measurement scan is made relative to a standard polished prism, at three different positions along the groove. A slight enhancement at the middle of the face is evident, as are the roll-offs at the peak and valley.

Using this method we scanned the left-faces of the teeth independent of the right-faces. Fig. 11 shows the results of a transmission scan from one side of a typical sawtooth crystal. It is possible to have a transmission that is better than our standard prism, hence a relative transmission greater than 100%. As can be seen from the figure, however, it was challenging to fully polish the sawtooth grooves all the way into the bottom of the valley and to the top of the peak. This manifests itself as a slight enhancement at the middle of the face, with a roll-off at the peak and valley. This roll-off is generally limited to 0.5–1.0 mm at the peak and valley, as indicated in the shape for each face shown in Fig. 11. A cumulative plot of these measurements, superimposing all faces for many sawtooth radiators, is shown in Fig. 12. The difference between the relative transmission and the average per face is plotted, where the average excludes a small region of roll-off at both ends of each face. This plot indicates the spatial uniformity of the polishing along the faces of the teeth. Fig. 13 gives the distribution of the average relative transmission per face. The width of this distribution indicates the repeatability of the sawtooth polishing process, on a per-tooth basis.

3.4 Radiation Damage in Fluoride Crystals

The crystals of the CLEO RICH are not expected to be exposed to significant levels of radiation. The RICH inner radius is 820 mm, and its outer radius is 1020 mm. At these radii, the CLEO-II detector saw approximately 0.05 Rad/day. This rate is expected to scale very nearly with instantaneous luminosity, so that in CLEO III the rate would be 0.1 Rad/day, or 37 Rad/year.[8]

---

[8] The scaling with luminosity is only valid at the outer radii of the CLEO detector, where the penetrating radiation is shielded only by the inner detector material. The radiation doses to which the inner detectors will be exposed will actually not
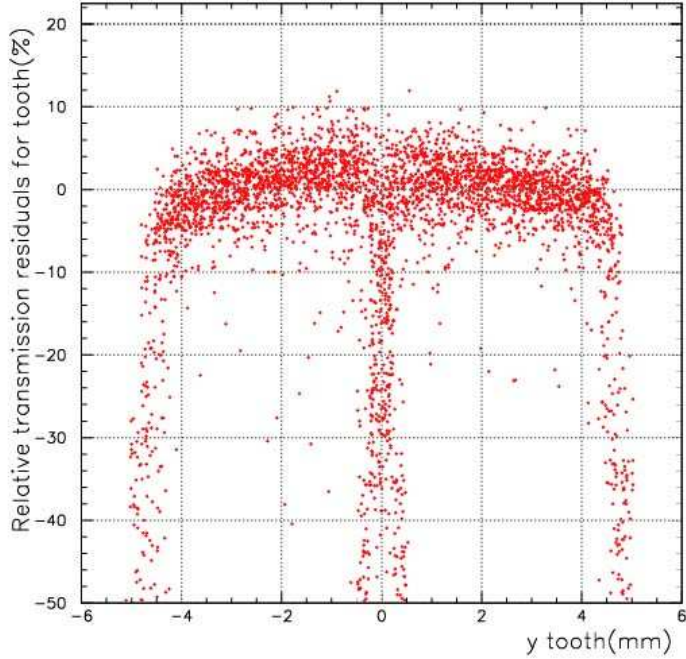
Fig. 12. Cumulative plot of relative transmission measurements for all faces of about 40 sawtooth crystals. The difference of the relative transmission from the average per face is plotted. Measurements are superimposed so as to indicate a single tooth, with the peak at 0 mm, and the valleys at $/pm$4.7 mm.
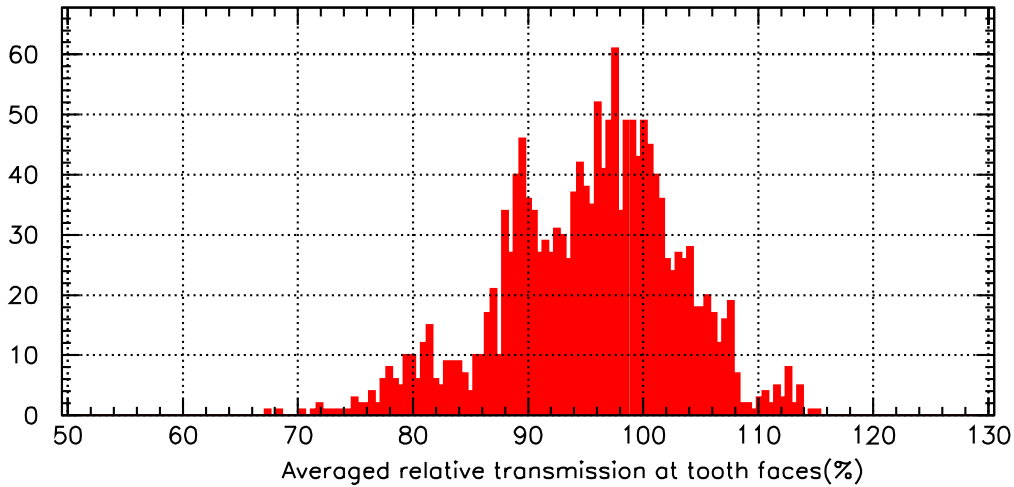

Fig. 13. Distribution of relative transmission per face, for all faces in about 40 sawtooth crystals. The average is calculated for each face, excluding a small region of roll-off.

In CLEO-c, the numbers are expected to be about a factor of four higher. We have investigated what effect could be expected on the transmission of the RICH crystals due to exposure to synchrotron radiation.

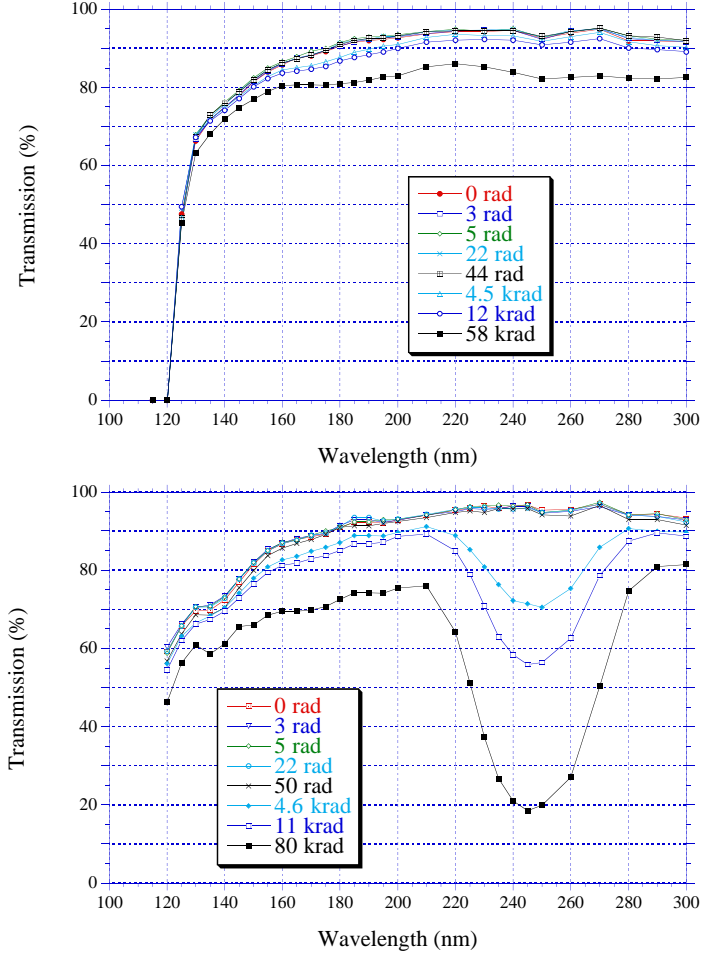differ much in CLEO III from those in CLEO-II due to improved shielding near the beamline.

20

Fig. 14. Transmissions of CaF_2 (top) and LiF (bottom) crystal samples irradiated by a ^{60}Co source, for different exposures, up to 80 krad.

Twenty CaF_2 and 20 LiF samples of the same thicknesses, as used in the RICH, were exposed for various times to a ^{60}Co source at rates of 200 to 5000 rad/hr. Transmissions of the samples were measured before and after the exposure. The transmissions did not appear to depend significantly on dose rate, only on integrated dose. A control sample that travelled with the dosed samples but was not exposed to the source did not experience transmission changes greater than 1% at any wavelength. Fig. 14 shows the transmissions of the crystals after exposure to the Co^{60} source. The observed absorption bands in the LiF at ~250 nm and 170 nm correspond to known color center formation centers [17,18], as do the 190 nm and 250 nm centers observed in the CaF_2 [19,20]. At the 100–500 Rad exposure expected in CLEO III and CLEO-c, however, the loss in transmission expected in our crystals would not exceed a few percent in the 135–165 nm range.

21

4 MULTI-WIRE CHAMBER CONSTRUCTION and TESTING

The main issues of concern guiding the construction of the multi-wire chamber photon detectors were: (1) field stability, requiring electrodes to be parallel over the full area of the detector, as well as have no local corona points, and high material cleanliness; (2) mechanical stress relief, to avoid cracking the thin CaF_2 windows or breaking an anode wire; (3) gas tightness, to prevent any VUV photon-absorbing gas from leaking into the expansion volume, or any impurities into the chamber gas; and (4) long-term stability, since in all practicality, the installed detector can never be accessed. Fig. 15 gives a schematic view of the multi-wire chamber.

To reduce dirt and dust, a clean room was set up, with air filtering, and the requisite cleanliness protocols (masks, nitrile gloves, booties, etc.). All chamber construction and testing of component parts occurred in this clean room environment. We purchased a set of three ten-foot long granite tables flat to better than 0.0005 inch over the entire table, in order to establish an accurate and stable reference. A mechanical prototype was constructed first, which was crucial in developing the detailed techniques and custom fixtures needed for the construction process.

The chamber construction procedure itself was a complex operation. The general technique was to assemble and test the two halves of each chamber (called the "wire plane" and the "window-plane") separately, then mate them together and test the completed chamber as a single unit. This procedure allowed careful construction of the three electrode planes, helped in problem diagnosis, and facilitated the production schedule.

For most of the construction procedures, two structural epoxies were used, as well as two sealant epoxies. All were chosen for their strong adhesion properties, viscosity prior to curing, as well as ultra-low outgassing attributes, as indicated in Table 1. All materials were checked for chemical comparability using a special chamber held at elevated temperatures [21].

4.1 Wire Plane Construction and Testing

The wire plane must be constructed in such a way as to maintain the 1 mm gap between the anode wires and the cathode-pads as uniformly as possible over the $\sim$2.5 m chamber length along which the wires are strung. Gain variation at the wires would result if this spacing was not uniform, as well as variation in the pad-gain, as a consequence of the capacitive coupling to the cathode-pads [5]. In addition, sparking could occur if the gain becomes excessively large at any place in the chamber. These requirement caused us to put a stringent

Table 1
Some special epoxies used in RICH construction.

Type	Epoxy	Consistency	Outgassing [22] %TML,%CVCM	Uses
Struct.	Armstrong A-12[a]	paste	1.11, 0.01	LiF, CaF$_2$
Struct.	Delta Bond 152-Q/B-4[b]	stiff	0.49, <0.01	G10, Ceramic
Sealant	Hysol RE2039/HD3561[c]	water	n.a.	Gas seal
Sealant	Torr-Seal[d]	stiff	0.92, 0.01	Gas seal

[a] Resin Technology Group, S. Easton, MA 02375.
[b] Wakefield Thermal Solutions, Inc., Pelham, NH 03076.
[c] Henkel Loctite Corp., Industry, CA 91746.
[d] Varian, Inc., Palo Alto, CA 94304 .
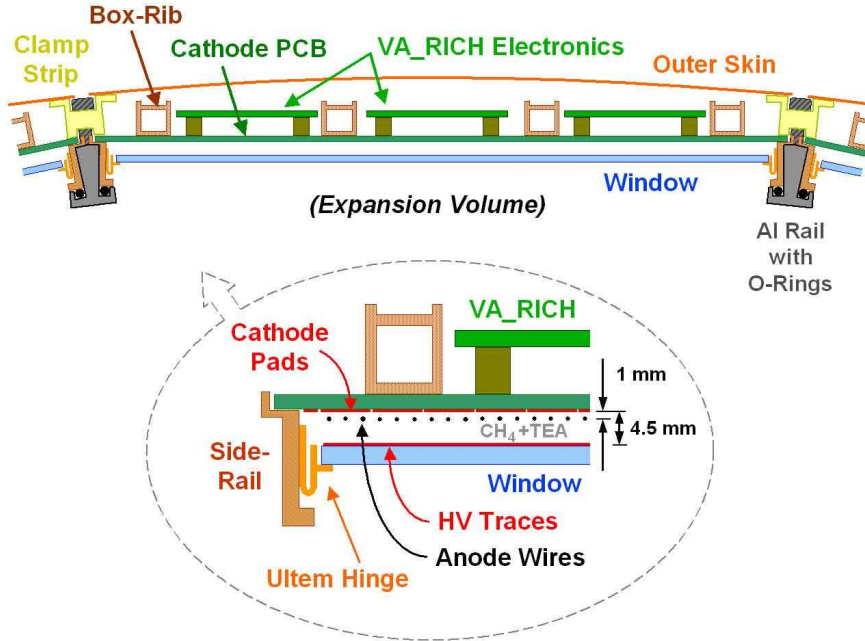
Fig. 15. Cross-section of full multi-wire chamber.

limit of 25 μm on the gap variation.

4.1.1 Cathode Board Design

The cathode board PCBs were designed to have cathode-pads on the front side and connectors for the electronics readout on the back side. Each board was about 205×615 mm^2 in area, and nominally 1.7 mm thick. Four boards made up a single chamber. Each contained two 24×40 arrays of pads. An 8×16 array of pads was routed to two linear connectors in a self-contained manner, so symmetry allows simple tiling of the plane.

As shown in Fig. 16, the pads on the front were connected to the traces on the back with small vias (0.5 mm diameter), which must all be sealed to prevent leaks. Rather than glue each via individually (∼8000 per chamber), an additional layer of prepreg was added to the top of the lay-up stack, which covered all vias and had cut-outs for connectors and ground connections. This design provided an excellent solution for sealing the vias.
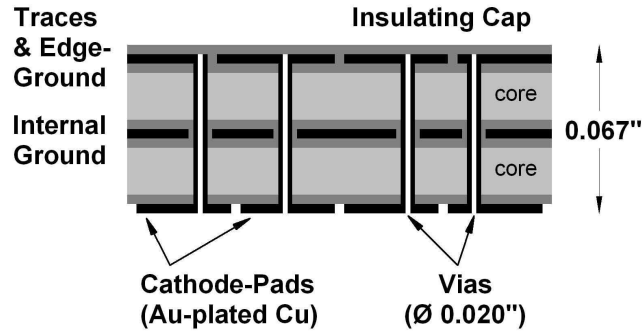

Fig. 16. Diagram of the cathode board PCB, showing the lay-up of the pads and layers. Black indicates a Copper layer, light gray a G10 core layer, and dark gray sheets of G10 prepreg. Vertical scale is proportional; horizontal dimension is compressed.

4.1.2 Cathode Board Manufacturing and Flattening Procedure

The large-area cathode board PCBs were manufactured, [9] under pressure in a stack in an autoclave. After manufacture, the boards were tested for continuity, inspected for irregularities, and measured to determine mechanical size and deformations. The connectors were then soldered to the board.

For a large-size thin PCB of this type, there were three major deformations from a geometric plane: longitudinal bow, transverse bow, and twist. The magnitude of the longitudinal and transverse bows were about 1.5 mm and 1 mm on average, respectively. The twist was small on this scale. In our design, the transverse bow was the most problematic deformation.

A flattening procedure was developed, in order to remove this bow. The boards were baked under weight while supported along the long edge. The thermal cycle was 2 hr at 150°C, followed by a slow 12 hr cool-down. The amount and placement of the ∼1 kg weights depended on the initial deformations of the board. The process was repeated as warranted. The effect of this procedure was to reduce the transverse bow to under half of its original value, on average. The longitudinal bow was not significantly changed.

---

[9] Speedy Circuits, Huntington Beach CA 92649.

4.1.3   Cathode Board Assembly

Four cathode boards were assembled into a plane by gluing them together end to end on the granite table—weighted, edge-clamped, and pad face down to assure geometric planarity of the finished pad array. [10] The end-joint between PCBs was specially reinforced: a "vee" cut was milled on the back to allow a larger contact area for epoxy and to ensure that no epoxy came through to make the front (pad) surface irregular. (See Fig. 17.) This joint was covered on the back by a G10 strip in a separate gluing operation for additional strength. The appropriate ground straps between boards were added. Measurements were made of the flatness to monitor the gluing procedure.

Next, the four fiberglass box rib structures were screwed to "strongback" into inserts previously glued into the box ribs. The strongback was made of full-length 1×2 inch aluminum box channels. The box ribs were then epoxied longitudinally on the back of the cathode PCBs. Enough glue was applied that any surface non-uniformities in the cathode boards or ribs would be accommodated by the glue. In addition, G10 cross-pieces were epoxied transversely between the ribs. (See Fig. 15.) The main purpose was to provide requisite stiffness to the thin cathode board, when mounted in its final configuration. A second purpose was to remove the residual deformations in the cathode board (the longitudinal bow being removed more effectively than the transverse bow). Excessive twisting, for example, would increase the possibility of breaking wires.

The strongback remained connected throughout the whole construction procedure until the completed chambers were attached to the cylinder superstructure.
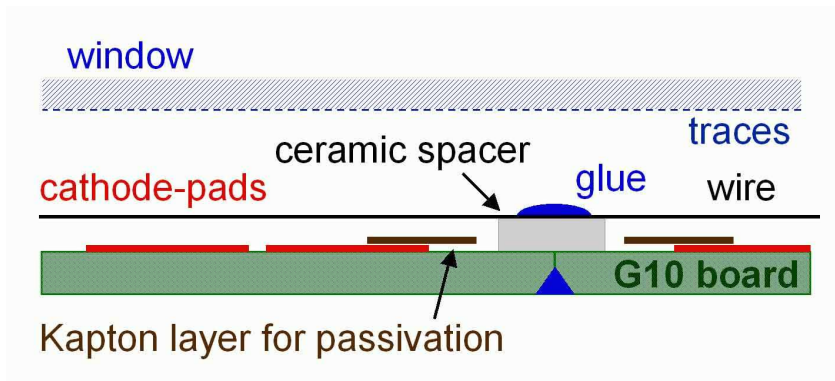

Fig. 17. Diagram of longitudinal cross-section of multi-wire chamber, showing the ceramic spacer and the end-joint reinforcement of the G10 cathode board PCBs.

A precision ceramic spacer was epoxied each 30 cm along the cathode plane,

---

[10] There was a variation up to 25 μm in the thickness of the etched pads themselves, from board to board.

near the window connections. This holds the wires at a precise distance from the cathode-pads, as well as allow for containment of the failure mode in which there was a broken wire. The ceramic spacer was cleaned before gluing, and care was taken in handling it, so as not to allow any grease or dirt to provide an eventual current path from the wires to the cathode-pads. The wires were eventually epoxied to the ceramic strip which had a slot running down the center to contain the glue bead. The area next to the spacer on the cathode board was passivated by a strip of Kapton, as indicated in Fig. 17. This extended over the edge of the nearest pad, and was done in order to remove the potential problem of any corona points that could lead to high voltage instability over time. Our experience with an early prototype showed that this was necessary.

The anode PCBs, on which the wires were to be soldered, were then epoxied into individually-milled grooves on top surface of cathode board, in order to have precision control of the wire to cathode-pad distance.

4.1.4   Wire Stringing

The chamber wires were strung on a custom-made jig, consisting of a PCB and a precision comb aligned and fixed at each end of a rail structure, approximately 3 m long (longer than a chamber). The 70 central field wires were 20 μm diameter Au-plated W wires[11] held at 60 g tension. The two outside wires would produce higher fields so we used larger diameter 30 μm Au-plated W wire[12] held at 90 g tension to keep the gain approximately at the same level as the central wires. Each wire was held at the appropriate tension by means of a frictionless pulley with a weight. The wire was carefully positioned in the comb using transverse locator screws. It was then soldered at each end to the PCBs. When done for all wires, a "temporary" plane of wires was created. As much as possible, a single spool was used for the field wires of a given plane.

This temporary plane was tested for wire tension using the standard resonance frequency method. Any wire out of tolerance (± 2 g) was replaced. Fig. 18 shows the distribution of tensions for a representative sample of wires.

4.1.5   Wire Transfer

After the cathode plane was prepared, as described above, the temporary wire plane was flipped over and lowered onto it by means of precision scissor jacks. This was a delicate operation, since the wires had to be aligned to the solder

---

[11] LUMA Type 861-60, W with 3–5% Au and 3% Re, LUMA-METALL AB, 391 27 Kalmar, Sweden.
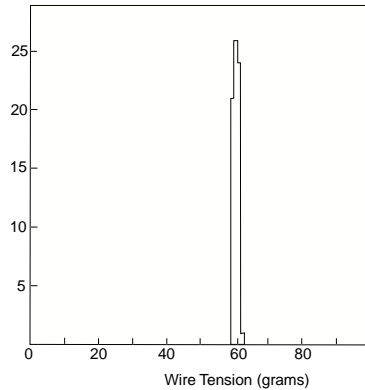[12] Type F-77, 4% Au, Philips Elmet Corp., Lewiston, ME.

Fig. 18. Typical distribution of tension in wires, as strung.

pads on the anode PCBs and just touching the ceramic spacers. When in position, each wire in turn was soldered to two consecutive pads on each end, approximately 5 mm in length, separated by 5 mm of non-pad surface. We chose to use solder with silver added. [13]

The quality of the solder joint was then assessed, and inspected for sharp points (important since the solder joints will sit in the chamber gas volume). The wire was cut behind the back solder joints, and checked for electrical continuity. Then anode PCBs were given a first cursory cleaning with isopropyl alcohol. The solder joints were covered completely in Delta Bond glue to prevent the solder from being attacked by the TEA in the gas. This process transferred the wires at tension from the temporary jig to the real cathode plane.

The anode PCBs were then populated with their requisite components, as indicated in Fig. 19. This was a mixture of discrete and surface-mount components. The novel feature here is that the large HV surface-mount capacitors (size 1812) were mounted on their *side* edge, in order to retain the tight-packing demanded by the wire spacing and the constraints on the overall chamber length. A technique was developed which used a special jig and both solder paste and solder cord, and this worked acceptably well for all chambers. Afterwards, the PCBs were brushed with isopropyl alcohol, and the electronic components tested.

The wires were then epoxied to the ceramic spacer. The glue bead was well-contained in a groove atop the ceramic spacer, such that the bead itself was smooth and there was no wicking along the wires. A bead of glue was also made between the two solder joints on the anode PCBs at each end, ensuring no loss of tension over time.

The last stage in the wire transfer procedure was a thorough final cleaning of the anode PCBs. This was accomplished by immersing the entire end of the

---

[13] Ersin Type Sn62, Eutectic, Tin/Lead/Silver, Multicore Solders, Westbury, NY 11590.
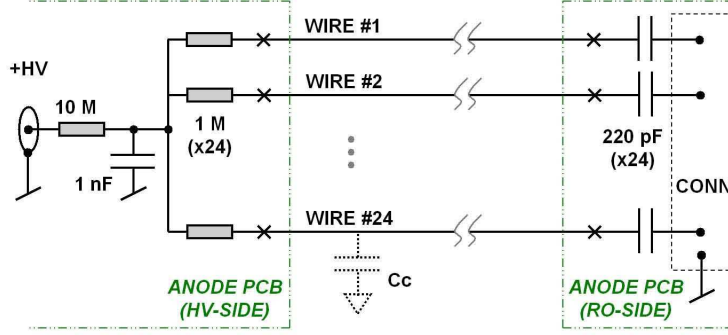
Fig. 19. Circuit diagram of one high voltage cell. There are three such cells per multi-wire chamber. The blocking and decoupling components are shown. The wire-to-pad coupling $C_c \approx 0.1$ pF/pad.

wire-plane in a large ultrasonic bath filled with isopropyl alcohol, and covering all solder joints. The wire-plane (via its strongback) was mounted on a wall at a 23° angle in order to submerge the anode PCB in the bath. Each end was bathed for 30 mins at a time, and repeated three times with fresh isopropyl alcohol. Afterward, it was rinsed with isopropyl alcohol and dry nitrogen. This was not a completely efficient procedure, since in many cases, there remained a whitish residue around some components afterwards. This is a well-known effect due to solder resin, and simply needs to be cleaned by hand.

4.1.6 High Voltage Testing

After ground connections were made, the wire-plane was placed into a polycarbonate testing box, filled with CH_4 gas and tested for high voltage stability. All wire-planes were tested to 1600 V, with ≤ 10 nA current draw, in conditions of ~22°C and <15% relative humidity.

In total, there were 35 wire-planes constructed. One was destroyed in subsequent testing, leaving 34 functional planes. They were stored in a low humidity tent until mating with the window-planes.

The wire connections have been very reliable (due to the conservative tension). One wire in the completed detector broke early in the operation due to the chamber exceeding the operating temperature, which went undetected due to insufficient slow control monitoring at the start of the experiment.

4.2 Window-plane Construction and Testing

After production of the windows as described in Section 3.2, the full window-plane was constructed. This consisted of a window frame into which the full-

length ladder of eight window segments was epoxied.

The individual window segments, wrapped in teflon, were epoxied in pairs. They were butt-jointed with Torr-Seal, with a well-controlled glue bead. The pair was held together in a custom-made jig, under gentle compression, during the curing period. The interior surface of the butt-joint was "painted" using Hysol. When completed, this procedure was repeated for two pairs, and then once again, for a full-length ladder of eight window crystals. [14]

The full window frame consisted of a long fiberglass side-rail, G10 end pieces, and an Ultem plastic hinge, all epoxied together, as shown in Fig. 15. The G10 end pieces had holes bored through for gas flow to the completed chamber.

The Ultem hinge was specially designed to allow some flexibility when the crystal window was glued to it, in order to take up any mismatch in thermal expansion between the crystals and the stiff frame. The full-length ladder of windows was lowered onto the frame, and glued to the Ultem hinge using Armstrong A-12. At the same time, a small metal foil was wrapped around the edge of each individual crystal window and glued to the interior trace bus-bar by conductive epoxy. On the exterior, this foil was soldered to a teflon-coated high voltage lead wire. [15]

After curing, another bead of epoxy (Hysol) was put on top of the existing one, in order to provide a secondary gas seal around the perimeter. Additionally, the butt-joints between window crystals were reinforced by gluing a narrow G10 strip over the joint, externally. This was again reinforced by a glue bead (Torr-Seal) on either side. The Torr-Seal was also used to tack the high-voltage wire along the frame. This operation may be seen in Fig. 20. The end-joints of the windows overlap the position of the ceramic spacers on the cathode plane to minimize the blockage of Cherenkov photons.

The critical mechanical item used in this construction procedure was a set of custom-made (multilayered) jigs, which established the proper referencing surfaces to hold the tolerance in window-to-cathode board spacing. In total, there were 34 window-planes constructed. After testing procedures, 33 usable planes were produced.

4.3 Full Chamber Construction and Testing

In the next step a wire-plane was matched with a mechanically suitable window-plane, and they were clamped together temporarily. The cathode-pad

---

[14] Half-plate windows were made into full-plate windows by the same technique.

[15] Gore Type F01A080 Wire, W.L. Gore & Associates, Inc., Newark, DE 19711.

Fig. 20. Construction operations being performed on two multi-wire chambers.

to window gap was measured at many points along the length of the chamber. The distribution about the nominal 4.5 mm gap size is shown in Fig. 21 for all chambers using approximately 32 measurements per chamber.
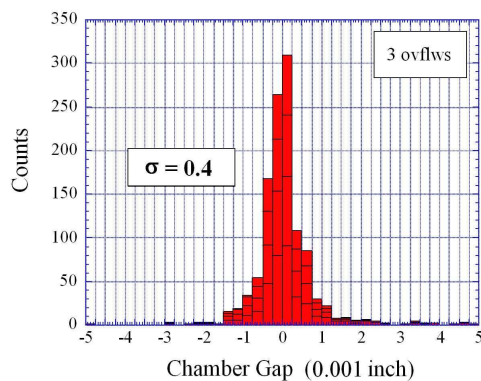

Fig. 21. Distribution of the residual about the nominal cathode-pad to window gap.

The mated chamber was tested with CH_4-TEA gas, with nominal high voltage on both wires and windows for a full month. Four special test boxes were used in this testing phase, so that tests could be performed simultaneously. The chamber was scrutinized heavily during this period. Relative chamber gain was measured from the wires, upon excitation by a ^{106}Ru β-source. Current draws were monitored. Problems were diagnosed and fixed. Typically, if the chamber drew more than 10 nA, it was opened up and cleaned of stray dirt or residual construction materials acting as corona points. These were the most prevalent problems.

If a mated chamber passed this test period, the given window and wire-planes were epoxied together and the chamber was completed. The full chamber was then tested again for a month, under these same conditions.

One problem encountered later, when the chambers were mated with the radiators, was leaking of chamber gas. This was attributed to certain of the fiberglass side-rails, which were epoxy-starved and microscopically split under small torsion applied during handling. This situation was rectified, using a rather painful procedure, that required painting a coat of Hysol epoxy over the side-rail, and reinserting the chamber before the glue dried; this often had to be repeated.

A total of 33 chambers passed all tests. On the average, this phase of construction took $\sim$0.5 months per chamber. Parallel operations allowed a maximum of eight chambers to be constructed in a single month.

The last stage in individual chamber construction was mounting the electronics chip-carriers and cables on the back. The hybrids (described in Section 7) were screwed into small standoffs epoxied to the connectors, thus attaching them with a squeezing action instead of pressing action which could deflect the cathode board and possibly break wires.

5   RADIATOR CYLINDER CONSTRUCTION

5.1   Inner Carbon Fiber Cylinder

The RICH Inner Cylinder has $12\,\text{m}^2$ of LiF crystals attached to a cylindrical $1.64\,\text{m}$ outer diameter carbon fiber support shell [23] of $2.48\,\text{m}$ length and $1.5\,\text{mm}$ skin thickness. The shell has mean density $1.42\,\text{g/cm}^3$, mean Young's modulus $E \simeq 70\,\text{GPa}$, and is built from wrapping multiple layers of pre-impregnated unidirectional tape [16] around a drum-shaped steel mandrel. After serving as the form for the carbon fiber tape during autoclaving, the mandrel provides mechanical support for the shell during transportation, radiator assembly, insertion into the Outer Cylinder of photon detectors, and installation of the entire RICH detector into CLEO.

The mandrel rotates on a shaft that allows the shell to be rotated to an arbitrary azimuthal position. A large box-beam frame [24] supports the shaft so that the total mass of the radiator system, including all its auxiliary mechanical fixturing, is $3500\,\text{kg}$.

---

[16] Type RS-3/AS-4 unidirectional tape, YLA, Inc., Benicia, CA 94510.

The radiator cross-section is essentially a 30-sided polygon ("triacontagon") with each side corresponding to a longitudinal row of 14 radiators. (Each row contains 13 full-sized crystals and two half-sized crystals at one end.) Construction was accomplished by first assembling and aligning rows of crystals and then attaching the rows sequentially to the support shell. All radiator assembly procedures are performed inside a class 100,000 clean room with typical 25% relative humidity to reduce the risk of contaminating crystal surfaces with particulate matter or excessive water vapor. Test crystals placed in the clean room were periodically measured for VUV transmission to verify that the ambient environment did no damage to radiator crystals.

To construct a radiator row, a set of 13+2 crystals were selected on the basis of VUV transmission and compatible mechanical dimensions. Each crystal was attached temporarily, by a $50\,\mu$m thick Kapton belt, to a picture frame jig that rests directly on top of it and that has vertical posts in each corner to provide for temporary attachment to a transport jig. Each crystal with its attached jig was then placed on an optical stage assembly with 6 degrees of freedom (3 orthogonal linear displacements and 3 Euler angle rotations). The 15 stage assemblies were all attached to a single rigid optical rail.

The open picture frame allows a pair of $2.2\,$cm diameter dowel pins to be placed directly on the crystal top surface. These pins support a precision level so that each surface is made horizontal to a typical angular precision of $150\,\mu$rad. A similar technique is used to limit vertical offsets between top surfaces of adjacent crystals to a precision of $\sim 50\,\mu$m.

A $100\,\mu$m clearance gap between adjacent crystals was reliably set by the thickness of the Kapton belts from adjacent crystal jigs. Pushing the same edge of each crystal flush against a set of tooling balls running parallel to the optical rail ensures that one edge of a crystal row was straight within $75\,\mu$m over its entire length.

After a crystal row has been aligned, a second "transport" optical rail is positioned over the crystal jigs. Quick-setting epoxy temporarily fixes the transport rail to the vertical posts of each crystal jig. The transport rail, along with the attached row of crystals, was then moved to the carbon fiber cylinder.

Linear translation optical stages positioned at opposite ends of the support shell near its surface at the "twelve o'clock" position receive the transport rail, as shown in Fig. 22. Reamed holes in these stages mate with dowel pins in the transport rail so that the axis of the new crystal row is aligned with the axis of the support shell. These stages eventually set the epoxy gap between the crystal bottom surfaces and the cylinder surface to $25\,\mu$m precision. Gaps

Fig. 22. Photograph of one row of crystal radiators being aligned on the inner carbon fiber cylinder. Previously epoxied rows are shown on the right half of the cylinder. The inner half of the end flange is visible in the forefront.

between adjacent crystal rows on the cylinder were controlled by the azimuthal rotation of the mandrel, set by a micrometer actuator to a precision of $\sim$ $50\,\mu$m.

After a crystal row has been appropriately positioned about the shell surface, Armstrong A-12 was applied to the shell just below the center of each crystal. No special preparation of the shell surface was performed. The crystal row was then lowered by the stages to make a nominal $150\,\mu$m gap between shell and crystal, forcing the epoxy to make a contact patch with nominal surface area of $100\,\text{cm}^2$. The jigging was left in place for a minimum of 8 hours before removal. The shell was then azimuthally rotated $12°$ to a new position and the entire alignment and epoxy process repeated until all 30 crystal rows were attached.

5.3   Radiator Transport

Care was taken to prevent the LiF crystals from experiencing excessive vibration or humidity during radiator transportation from its construction site (Dallas, TX) to the detector integration site (Syracuse, NY). A dedicated temperature-regulated shipping truck was used for the 2500 km trip. A local atmosphere close to 0% relative humidity (measured as <1%) was achieved by erecting a temporary plastic film cocoon around the radiator and flowing dry N_2 gas through the cocoon from gas bottles attached to the shipping frame.

Air bags attached to the four corners of the shipping/rotation fixture cush-

ioned the radiator against mechanical shock and vibration. Acceleration of the radiator and temperature inside the truck as functions of time were measured, digitized and written to local non-volatile memory by special instrumentation [17] installed on the mandrel support frame. No damage to the radiator was observed at the trip's conclusion.

6   SUPERSTRUCTURE CONSTRUCTION

The guiding principles for the design and construction of the full cylinder mechanical superstructure were: (1) low mass, so as not to degrade the excellent performance of the electromagnetic calorimeter surrounding the RICH; (2) no internal obstructions, so as not to shadow the photon detectors; and (3) an excellent gas seal.

The overall design of the superstructure consisted of an "Outer Cylinder" for the multi-wire chambers, and an "Inner Cylinder" for the crystal radiators. The expansion gap separated these and was contained by two large end flanges [12].

6.1   End Flanges

For construction purposes, the two annular end flanges were each made of two concentric parts, as shown in Fig. 23. The outer half was a structural element for the Outer Cylinder, and the inner half was fixed to the carbon fiber shell of the Inner Cylinder. These two parts fit together with an double gas seal, as described below. The end flanges were made of structural aluminum alloy, and coated on the interior surface by low-outgassing black paint.

6.2   Outer Cylinder

The construction of the Outer Cylinder used a scaffold, on which the multi-wire chambers were mounted, as can be seen in Fig 24. It had long thin aluminum rails supported between the outer halves of the end flanges. The rails were machined to fit between the chambers, and contained an O-ring groove that was the primary gas seal for the expansion gap at the Outer Cylinder. As it was not very stiff but had to maintain the requisite compression on the O-ring, a clamp-strip was used to squeeze the chamber on the O-ring, with screws spaced on 1 inch centers. Hence the chambers themselves effectively

---

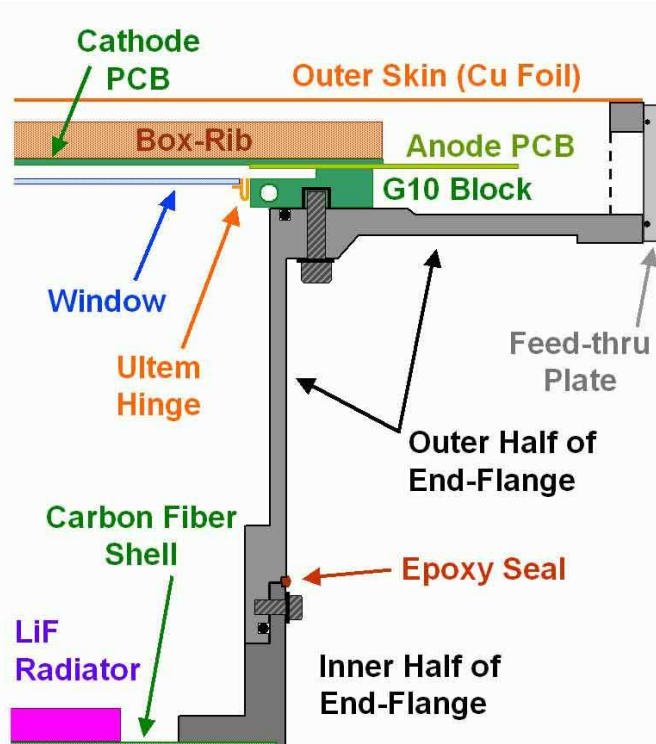[17] Model EDR-3C, Instrumented Sensor Technology, Inc., Okemos, MI 48864.

Fig. 23. Cross-sectional view of one end of the RICH detector, showing end flange construction.

formed the outer radius of the detector. This is another reason why the box rib reinforcements were needed.

Fig. 24. Photograph of Outer Cylinder during construction, supported on the A-Frame, with "dummy panels" in place.

During assembly, the Outer Cylinder was held on a large custom-designed A-Frame structure with three-point kinematic mounts, allowing free rotation

of the cylinder. Initially, the inner area of the end flange was plugged, and the thirty chamber spots were taken up by "dummy panels," stiff blanks that allowed for gas tightness testing of the cylinder. In this condition, the out-of-roundness deformation was measured, as shown in Fig. 25, to have a small eccentricity.
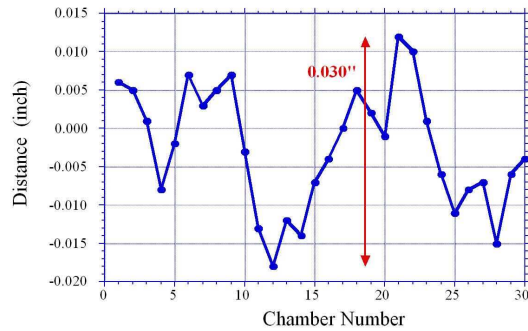
Fig. 25. Out-of-roundness deformation of end flange, under no-load condition.

As chambers were completed, the dummy panels were removed and the chambers were mounted on the cylinder. A photograph of the interior during this procedure is given in Fig. 26. It was only at this time that the strong-backs could be removed. Leak-checking could then be done using He gas for high sensitivity. This was particularly important at the corners of the long single O-ring seal around the perimeter of the chamber. Often, the joints and corners had to be hand-worked to seal at the level of 10^{-4} ml/s.

Fig. 26. Photograph of inside of Outer Cylinder with photon detectors installed.

The Inner and Outer Cylinders were mated in a precision mechanical process. The inner half of one end flange was first epoxied to the carbon fiber shell while the other inner flange was free. The Outer Cylinder was rotated azimuthally to align the fixed inner-half flange with its corresponding outer half and O-rings were installed in both outer flanges. The Inner Cylinder remained on the mandrel and slipped into the Outer Cylinder, riding on two large box-beams. The halves of the end flanges were screwed together, providing the mechanical coupling between the Inner and Outer Cylinders. An O-ring provided the primary gas seal at this junction. Following our dictum to use redundant gas seals on all mated surfaces, a secondary gas seal was made by a glue bead around the joint. The previously free inner half of one end flange was epoxied to the carbon fiber shell as the mechanical connection was made.

Thereafter, the completed structure could be supported by the mandrel. It was then transported for installation in CLEO by a method similar to that used for the radiator cylinder. Chambers and gas seals were then all tested again, in situ. After additional iterations of hand-working and testing, the expansion volume was sealed. Most leaks occurred when the inner and outer cylinder were mated.

7 READOUT ELECTRONICS

7.1 System Description

The CLEO RICH electronics design is driven by two important considerations. First of all, we need to operate the chambers at moderate gain, to improve the stability of operation and the lifetime of the detector system. This requirement is very important as the system is designed to operate throughout the lifetime of CLEO without any access for repair. In this regime the single photon response of the MWC used as photon detectors has an exponential distribution, as shown previously in Fig. 5. Thus, low noise is a critical requirement to maintain good efficiency. On the other hand, the exponential distribution spans a wide dynamic range. Moreover we would like to be able to reconstruct the charge deposited by a minimum ionizing particle, shown as the bump on the right-hand side in the distribution of Fig. 5. This implies that a wide dynamic range is also very important.

The cathode-pad segmentation is such that the charge signal induced by the avalanche is spread around more than one pad, thus analog charge weighting

produces a better spatial resolution and also allows for easier separation of the charge clusters produced by two nearby photons. Thus we chose to implement an analog readout.

Fig. 27 shows a schematic view of the readout architecture for a multi-wire chamber. Each chamber is divided into four sectors. Each sector contains three daisy-chained rows, connected with 50-conductor shielded cable to the back-end electronics, located in VME crates about 18 meters from the detector cylinder.
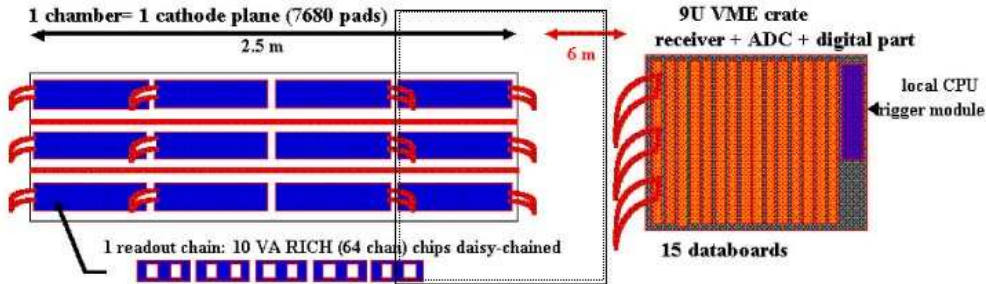

Fig. 27. A schematic view of the readout architecture for a single multi-wire chamber.

The front-end hybrids, shown in Fig. 28, are mounted on the back of the cathode board in a mother board-daughter board configuration. Five hybrids are daisy chained and share the same bias sources. Each hybrid has an independent differential output for faster data processing.
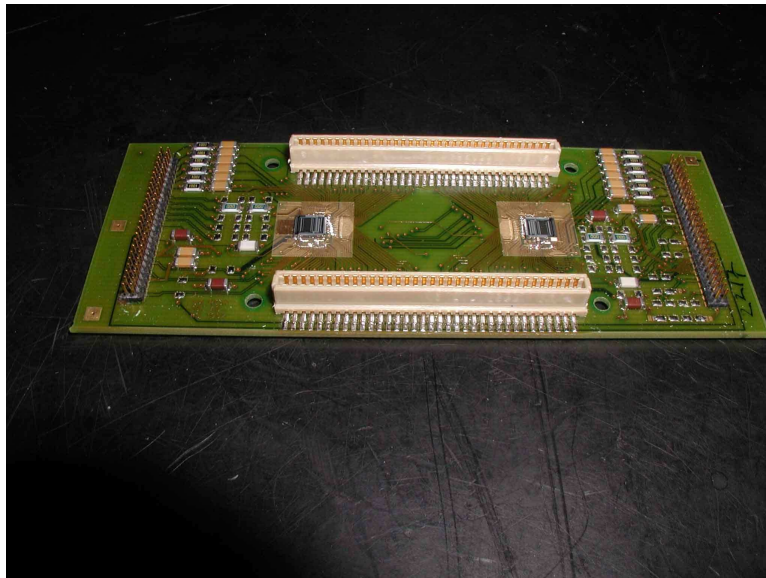
Fig. 28. Photograph of the front-end hybrids of the CLEO RICH. Two VA_RICH ASICs are visible, which are wire-bonded to the PCB. No protective caps are used.

A photograph of a quarter-section of the cathode board with the hybrids attached is shown in Fig. 29.
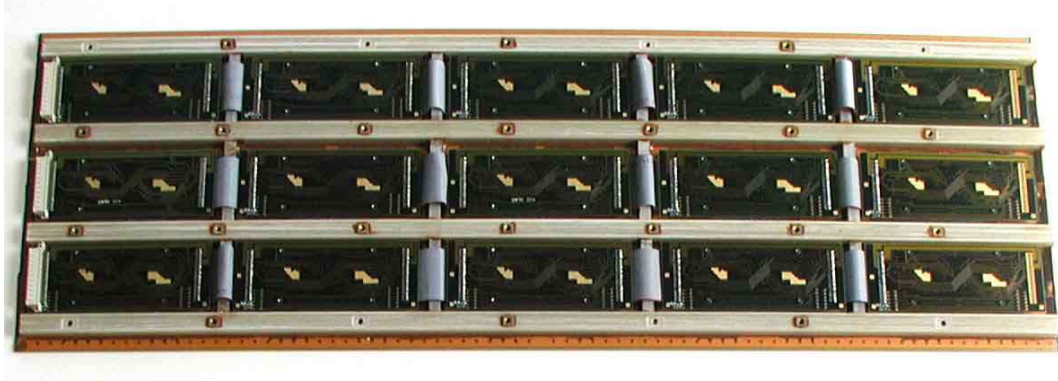
Fig. 29. Photograph of 1/4 of a cathode plane.

7.2 The Front-End ASIC

The heart of the front end electronics is the VA_RICH ASIC. It was designed for our application by the engineering team at IDE AS, Norway [13], and is an adaptation of the basic design of the very successful VA family, originally developed to process the signals of silicon microstrip detectors, tailored to our noise and dynamic range requirement.

Fig. 30 shows a conceptual diagram of this device. It features 64 individual channels including a semi-Gaussian preamplifier and shaper circuit. The peaking time can be adjusted by changing the biases of the shaper circuit around a typical value of 2 μs. We tuned the peaking time to match the time when a Level 1 decision is achieved. This section is followed by a sample and hold circuit, which is designed to hold the peak level out of the shaper until the output multiplexer is ready to transfer this level as a differential current. The individual inputs are connected through a 64:1 multiplexer to a calibration circuit, which allows injection of a test charge into each individual channel. The ASIC is implemented in 1.2 μm AMS CMOS technology.

The equivalent noise charge dependence upon the input capacitance was measured on prototype single chip hybrid carriers, using a set of calibrated capacitors. The measured performance matches the predictions from the ASIC simulation [25]. In our application, we expect a total equivalent noise charge of 300 e$^-$, without the cathode boards connected. Fig. 31 shows the analog output voltage on 500 Ω resistors. Saturation occurs at an input charge level of 80 fC. In the linear region, the preamplifier and shaper gain is 40 mV/fC, for a load of 500 Ω.
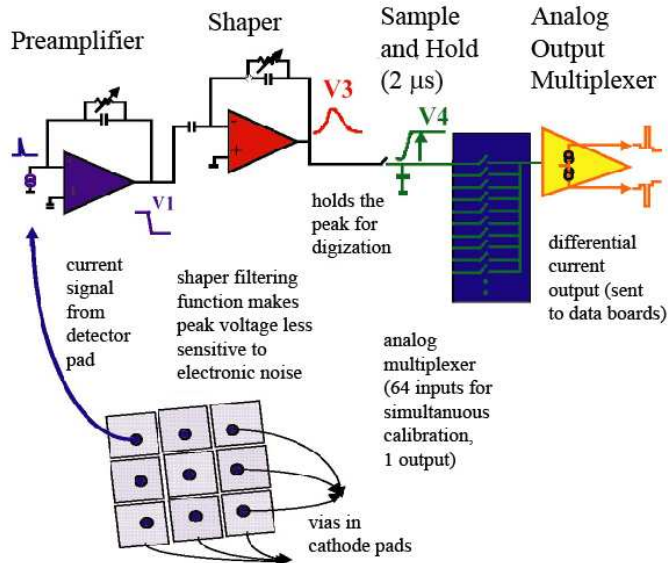
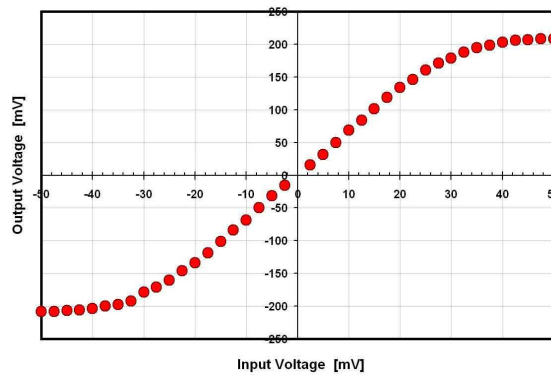Fig. 30. A conceptual diagram of the VA_RICH ASIC.

Fig. 31. Typical VA_RICH output response curve.

7.3 Bench-Test Characterization

The total number of hybrids produced was 2200, over a period of two years. The hybrids produced were tested for functionality at IDEAS and then shipped to Syracuse for more complete characterization. Our tests involved a noise measurement by taking pedestal data, followed by a detailed mapping of the individual channel gain with calibration pulses of different amplitudes. Only 1800 were installed in the detector.

The noise measurement required great care in the grounding and shielding of the hybrids and careful routing of the analog power supplies. Our goal was to achieve a noise of the order of 400–600 e$^-$ with a simple and relatively quick set-up of the measurement.

After this initial characterization, we performed a burn-in test of the hybrids, maintaining them biased in their nominal working point at elevated tempera-

ture (70°C) and performing electronic calibration cycles at regular intervals. In order to perform these tests at a rate compatible with our installation schedule, we produced a dedicated set-up where 32 hybrids could be biased and monitored in parallel. After one week in the burn-in set-up, the hybrids were tested for noise and gain with a quicker calibration procedure. The hybrids that were rejected upon this procedure were only a few per thousand.

7.4 CLEO RICH Data-Boards

Fig. 32 shows a picture of the CLEO RICH data boards. They are 9U mixed analog and digital environment boards that perform several very complex functions. Note that the board is physically composed of two different sections. The first is an analog section, providing the biases needed for the functionality of the VA_RICH ASIC, the transimpedance receivers, 12-bit ADCs digitizing the serial analog information, and slow control monitoring ADCs. The second is a pure digital section, based on a common CLEO data acquisition framework, and containing two components specific to our application: a sequencer, based on the ALTERA MAX FPGA, that contains the firmware necessary to operate the VA_RICH ASIC, and an Analog Devices ADSP-21061 DSP, used to perform the common mode suppression and data sparsification described below.
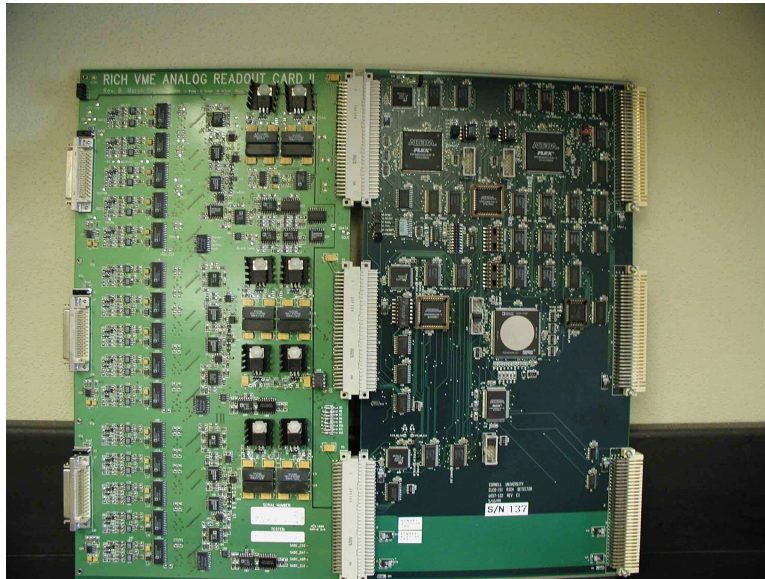

Fig. 32. Photograph of the CLEO RICH Data Boards: Analog board on the left, Digital board on the right.

The analog section features 15 receiver channels, organized into three cells sharing the same ribbon cable interconnection to the front end hybrids. Each cell encompasses dedicated ±2V analog power and several DACs that allow the adjustment of the bias currents and voltages that influence the working

41

point of the analog front end, as well as a slow control section that monitors the values of these voltages and currents, and the temperature on different locations of the detector cylinder and on the data boards themselves. In addition, local pulse generators are used for the electronics calibration. All the cells share a common regulated $\pm 2V$ digital section.

When an event occurs, all the 15 channels in a board receive the synchronous serial information from the corresponding hybrid. In order to simplify the digital section the 5 ADC channels in a cell are multiplexed into a common FIFO buffer, with an offset of 23.4 ns, determined by the local 42 MHz clock.

To maintain the low thresholds that are required to optimize the efficiency, the hardware common mode noise suppression algorithm is crucial to suppress the adverse effects of coherent fluctuations of all the channels in an ASIC.

8 SUPPORT SYSTEMS

8.1 Gas System

The gas system supplies several distinct volumes. The system must: supply CH_4-TEA to 30 separate chambers, supply ultra-pure N_2 to the expansion volume, supply ultra-pure N_2 to a sealed single volume surrounding all the chambers, called the "electronics volume," since this is the region where the front-end hybrid boards are present. In addition we need to test the CH_4-TEA mixture for the ability to detect photons and test the output N_2 for purity.

It is of primary importance that the gas system must not destroy any of the thin CaF_2 windows. We use computerized pressure and flow sensors with programmable logic controllers (PLC).

8.1.1 System Design

The performance and mechanical integrity of the CLEO III RICH are critically dependent on the performance of its gas systems. In order to achieve its design resolution, the RICH must efficiently detect 14-21 photons emitted by charged tracks traversing the radiator. The efficiency of the RICH depends on the expansion volume transparency. The photosensitive detector gas and transparent nitrogen of the expansion volume are separated by fragile windows on the inner faces of the detector modules. These windows could be destroyed by a slight pressure difference between these volumes (of order 15" H_2O). Such an overpressure would be catastrophic to the RICH.

The gas systems were carefully designed to protect against such damage. A highly automated design was chosen in order to minimize the possibility of operator error and to provide fast response to dangerous conditions. Most valves are controlled by the automated control system and most sensors are read out and monitored electronically.

The two major subsystems are the expansion volume gas system (EVGS), which purges the expansion volume with a large flow of ultra-pure nitrogen, and the detector gas system (DGS), which supplies the thirty detector modules with photo-sensitive methane/TEA gas. Pressures in the detector and expansion volumes are referenced to atmospheric pressure. Both the EVGS and DGS employ triply-redundant overpressure and underpressure protection. The first tier of protection is based on readings from pressure transmitters connected to the expansion volume and each of the thirty detector volumes, and has trip points at +0.75" H_2O and -0.5" H_2O. The second is based on readings from pressure switches which have trip points set at +1.5" H_2O and -1.0" H_2O. The final level of protection comes from mechanical relief valves with set points at +2.5" H_2O and -1.5" H_2O. Valves which perform the most critical operations, such as those which shut off the gas inputs, are equipped with position indicating sensors and, in the most critical, redundant valves are implemented.

8.1.2 Control System

All critical operations of the RICH gas systems are controlled by a programmable logic controller (PLC). The PLC is an industrial control system designed to be reliable and modular. The control system utilizes 112 analog input, 8 analog output, 96 discrete output, and 128 discrete input channels. The gas system is controlled through a small number of buttons on the main control panel.

The basic operation of the EVGS and DGS is similar. Each has four states of operation: RUN, IDLE, STOP, and ALARM. RUN mode is the normal operating state of the system. In this state gas flows through the detector and the pressure is actively regulated by the PLC at 0.5" H_2O to an accuracy of ±0.02" H_2O. IDLE mode is similar to RUN mode except that the pressure is not actively regulated. IDLE mode is used in the system start up sequence. ALARM mode is the safe state to which the system defaults in case of an emergency. In this state, the input gas flow is shut off and the exhaust side of the detector is opened to track atmospheric pressure. After the system is stopped by an alarm it is important that it be restored to RUN or IDLE mode as soon as possible to prevent degradation of the CaF_2 and LiF crystal transparency when exposed to ambient humidity. After the offending condition is fixed, alarms may be reset using a button on the control panel. When the alarm is cleared, the system changes to STOP mode, which has the same

physical configuration as ALARM mode. The system start up sequence is fully automated and is initiated by pressing a single button. The start up sequence consists of a purge of the input lines, followed by a ramp of the input flow, and finally a ramp of the pressure. All transitions in the system are gradual in order to protect the RICH from possible pressure spikes.

All critical components of the gas system are powered through an uninterruptable power supply which is backed up by a diesel-powered generator.

Interfaces to the operator and to the CLEO III detector control system are provided through the gas system monitor (GMON), consisting of LabView^{TM} [26] programs running on a PC. The GMON programs collect sensor readings, status, and alarm information from the PLC which it displays in several "active schematics" corresponding to each of the major components of the EVGS and DGS. The GMON relays this information to the CLEO III slow control system.

The GMON also handles the display of alarms. "Fatal" alarms are generated by the PLC and result in the system defaulting to ALARM mode in order to protect the system from damage. All other "non-fatal" alarms are generated by the GMON code, which monitors the status of all system parameters. The system is heavily instrumented with sensors in order to allow problems to be easily identified and repaired.

The GMON programs are also used to control some non-critical operations of the gas system, such as the gas quality monitoring, and to set some system parameters. The gas system does not depend on the PC or GMON programs in order to run, however.

8.1.3 Expansion Volume Gas System (EVGS)

It is critical that the purity of the expansion volume be maintained in order for the RICH to achieve its design resolution. Most impurities will absorb the UV photons before they reach the detectors and must be kept below a few ppm concentration. This purity is obtained by flowing nitrogen at a rate of approximately 1500 ℓ/h in a single-pass configuration. Boil-off from liquid nitrogen is used as the source for the expansion volume gas. Most of this system is constructed from electropolished stainless steel and other materials with low vapor pressure in order to minimize impurities.

Nitrogen gas from the dewar is processed by an automated purifier subsystem. This purifier injects a regulated flow of hydrogen corresponding to 40 ppm, which reacts with the oxygen inside a catalyst cartridge to form water. A slight excess of hydrogen is acceptable since it is known to be transparent over the wavelength range of interest. Water and other large molecules are

44

removed by a large molecular sieve trap. The molecular sieve trap must be regenerated occasionally by baking at 300° C for a day. The purifier subsystem contains two parallel purifiers to allow for continuous operation while one of the sieves is being baked. The PLC controls the flow ramping and switching between purifiers as well as the temperature control and gas purge for the baking sieve.

The operating flow of nitrogen to the expansion volume is set with a manual metering valve near the input to the expansion volume. Gas exiting the expansion volume passes through ten 1/2" stainless steel lines to a 1" manifold outside of the CLEO III solenoid return yoke, where pressure is regulated by a PLC-controlled metering valve based on feedback from a pressure sensor.

8.1.4 Detector Gas System (DGS)

The detector gas system is responsible for providing thirty separate photon detector volumes with a mixture of methane and TEA. Because TEA is corrosive to most materials, 316 stainless steel components were used wherever possible. Any other materials used in the system were first subjected to stringent chemical compatibility tests.

TEA vapor is introduced into the stream of methane gas by bubbling it through liquid TEA at 15° C. The TEA bubbler system is automated using programs on the PLC for reliable and continuous long-term operation. It utilizes a temperature-controlled bubbler chamber and elevated TEA reservoir with enough TEA for approximately two months of operation. The level of TEA in the bubbler chamber is regulated by the PLC which fills from the reservoir as needed. The reservoir may be depressurized and filled without interrupting the operation of the system. Sensors monitor the level and temperature of the TEA in the bubbler and the level of the TEA in the reservoir and notify the user when refilling is required.

In order to provide adequate pressure control, it is necessary to supply gas to the chambers in a parallel configuration rather than in series. The flow is split into thirty separate streams to provide even flow to all 30 detectors. The flow in each branch is set manually and monitored electronically. The flow is ramped up and down automatically during start up and purge operations. A total of ninety 1/4" stainless steel lines pass through the CLEO III solenoid return yoke steel to connect to the thirty photon detector modules: one input, one output, and one pressure sensing line.

Exhaust from the thirty modules is collected into a single exhaust manifold. Gas from this manifold passes through a PLC-controlled pressure regulating valve which maintains the average pressure of the thirty modules at 0.5" H_2O.

8.1.5 Gas Quality Monitoring

A nitrogen transparency monitoring system measures the UV transmission of the expansion volume gas as a function of photon wavelength. Monochromatic light is produced by passing light from a deuterium lamp through a computer-controlled monochromator. The monochromatic photon beam passes through a gas sample tube and is detected by a photomultiplier. The sample tube can be switched to sample the expansion volume exhaust gas or an ultra-pure argon reference gas. A comparison of these two gives the transparency. The GMON controls the transparency monitor and other gas monitoring devices. Automated transparency scans are taken once per day. Graphical panels allow the user to configure the scans and view the results.

Oxygen is the most likely and problematic contaminant, since it absorbs strongly at 150 nm. The oxygen concentration of the output gas from the expansion volume is also monitored using a precision oxygen sensor.

The CH_4-TEA mixture is monitored by an electron capture detector. This device consists of a cylindrical proportional drift chamber which utilizes a beta source to produce ionization. Electrons produced near its outer diameter drift through a ~ 5 cm long path to an anode wire at the center of the chamber where they are collected. A 0-5 VDC signal proportional to the time-integrated drift current is monitored by the control system. Impurities or changes in the gas composition can be detected as a change in the output of this device.

8.1.6 Electronics Volume Purge System

The gas system also provides a purge flow of nitrogen gas around the electronics volume of the RICH in order to minimize the concentration of impurities adjacent to the gas volumes of the RICH. This helps to reduce the infiltration of oxygen into the expansion volume.

8.1.7 Performance

The gas system has been in operation since the early commissioning of the RICH and has been running in its final form since the Summer of 1999. The most critical aspect of its performance is that it has protected the extremely fragile CaF_2 windows from damage. It has delivered nearly continuous service for several years, with only a few short down-times for repairs. Identification and diagnosis of problems has been straightforward due to the wealth of information provided by the system.

The expansion volume transparency exceeds the specifications for the RICH design. The EVGS typically delivers transparencies of >99.5% at 150 nm, as

shown in Fig. 33. This wavelength is near the peak of the RICH sensitivity and is particularly vulnerable to oxygen contamination. The recovery time of the expansion volume gas system is quite short due to the high purge rate and careful choice of materials. After exposure to air, the expansion volume can typically be restored to acceptable transparency within a half day.
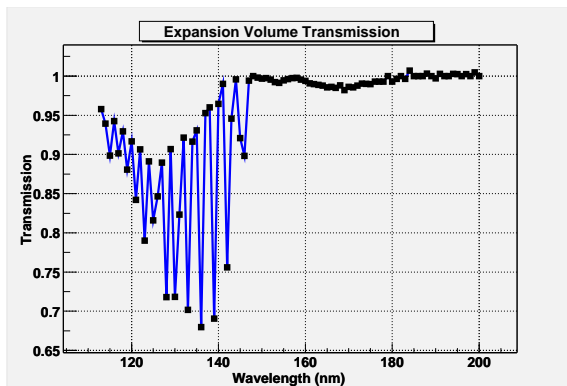

Fig. 33. A typical spectrum of the expansion volume gas transparency. The RICH response is centered at 150 nm and extends from approximately 135 nm to 165 nm. The structure below 150 nm is due to the vibrational-rotational absorption bands of nitrogen. The transmission at 150 nm is greater than 99.5%. (Note the suppressed zero of the vertical scale.)

The RICH photon detectors show no evidence of aging due to reactions of TEA with materials in the gas system and RICH. The DGS has provided reliable and simple operation. In particular, maintaining and filling the liquid TEA bubbler has proved to be quite simple and trouble-free.

The highly automated design of the RICH gas system has proved to be very effective at protecting the RICH and simple to operate. It has exceeded expectations of performance and reliability.

8.2 High Voltage System

The High Voltage System for the CLEO RICH was required to supply 90 channels of anode field wire voltage (about +1500 V) and 240 channels of cathode window trace voltage (about −1200 V), with a current monitoring and trip circuit on each channel. The system was based on the LeCroy ViSyN System [27], and consists of a Model 1458 mainframe containing slots for 16 Model 1469 modules, which have either positive or negative polarity. In our implementation, we use 5 positive and 11 negative modules. The module outputs are ganged together such that there are eight HV channels per so-called "bulk" connector, a specially-designed LHV connector. There are three bulk connectors per module. The system allows voltage setting at the bulk connector level, so each channel in the bulk connector has the same voltage,

but may have different current trip levels. The channels fan out to a patch-panel so the proper high voltage can be routed to each chamber channel. The value of the voltage setting on each of the 330 detector channels was determined by an optimization procedure, as discussed in Section 9.2.

Control of the high voltage system is accomplished by a stand-alone server program, on a dedicated linux station, that is integrated with the CLEO DAQ System in order to synchronize the state of the system with accelerator operation.

Ramping of voltages are made at rates of 40 V/s (increasing) and 50 V/s (decreasing) for both polarities. Care is taken to raise all voltages in a given chamber simultaneously, in order to minimize electro-mechanical deflections. All channels have current trip levels set to 10 μA, and are monitored at a rate of $\sim$2 kHz. Individual channel status, currents and voltages are read back and monitored as well. Any currents or voltages out of tolerance will cause an alarm, requiring immediate operator intervention. During detector operation, communication between the server and the mainframe is maintained via TCP/IP, and the status of all voltages and currents is displayed in a representational color-coded GUI.

8.3   Cooling System

The total power output of the VA_RICH chips is approximately 360 W. In order to provide heat removal necessary for the mechanical stability of the chambers, four nylon cooling tubes run over the back of each chamber, and are each modestly thermally coupled to the VA_RICH hybrids by two-component RTV.[18] Supplying these tubes with the hydrocarbon coolant PF-200IG is a specially-designed CLEO cooling farm [28]. This coolant is used rather than water because of concern that a leak could reach the water sensitive CsI crystal, which would melt; an additional advantage is that PF-200IG is non-conductive. The RICH cooling circuit is one of several driven by the cooling farm through active-manifold platforms, with a coolant reservoir temperature of 18°C and flow rate of $\sim$1 ℓ/min. Each RICH chamber line is equipped with an embedded tip-sensitive $100\,\Omega$ platinum resistance temperature sensor (RTD). For these RTDs, an array of "hockey-puck" style 4–20 mA transmitters route signals to a custom-built multiplexer circuit used to read out these transmitters every 10 s. The temperature signals are fed into a small logic controller for real-time control and monitoring. The typical range of exit temperatures from the 30 chambers when in operation is 21–23°C, each held stable to ±0.5°C.

---

[18] RTV 577 / RTV 9811, GE Silicones, Wilton, CT 06897.

The status of the cooling system is continuously monitored by a LabVIEW program which provides web-based diagnostic tools for real-time viewing of the performance parameters on site and monitoring worldwide.

8.4 Slow Control System

A bit-serial data bus was implemented on the P3 connector on the RICH AVME data board using differential signaling technique. This bus is referred to as the SBUS. The maximum transfer rate of the SBUS is approximately 1 Mbit per second. Each RICH VME crate is equipped with one SBUS crate controller. Each SBUS crate controller can be addressed uniquely. All eight RICH VME crates are daisy chained to one SBUS controller module located in a separate SBUS crate at the pit level.

The SBUS system is responsible for monitoring the operational status of the VA_RICH chips as well as that of the AVME data board. Important quantities such as the reference voltages, the reference currents, and the temperature on the chip carrier chain inside the RICH detector are being monitored periodically through the SBUS system. Analog signals from the RICH detector are converted into digital signals with a 10-bit ADC (TI TLC1542/3CDW) on the AVME data board for the SBUS read out. The SBUS can also be used to download some of the EEPROMs on the DVME data board.

A server program running on an on-line computer communicates with the SBUS controller module via CORBA calls. A monitor request is sent out every 15 minutes. This sampling interval is programmable and was chosen to ensure both adequate monitoring and maximum system wide stability. The data are shipped back to the server, archived locally in plain text files and then processed to provide information on the front-end electronics status in an easy-to-read HTML format on a Web server.

9   OPERATING EXPERIENCE

The CLEO RICH detector has been in operation since September 1999. All but $\sim 2\%$ of the detector is functioning for data-taking. We lost 1.7% due to the breaking of one wire after about one year of operation due, most likely, to the un-monitored heating of chamber due to problems with slow control software. We have also lost 2% of the electronics chips and suffered one broken output cable, so the total number of lost channels is $\sim 5\%$.

In order to ensure proper functioning of the RICH over the long period of its operation, a series of calibration and monitoring activities are performed periodically as a part of its normal operating procedure.

To ensure the highest detection efficiency of the VA_RICH chips, the electronics pedestals need to be measured routinely. This is done by performing a special calibration procedure called "SmallCal." During a SmallCal, the VA_RICH chips are set in calibration mode and the electronics noise from all 230,400 electronic channels are read out. The pedestals are then calculated on-line and loaded to the VME crates to be used for sparsification during successive data-taking runs. This SmallCal procedure is carried out regularly every eight hours.

Another type of calibration, the WirePulse run, is performed once per week. The purpose of the WirePulse run is to measure the response of the RICH electronics to a given input signal. During a WirePulse run, the anode wires are pulsed with a sequence of several predefined waveforms of differing amplitudes. The output from all electronic channels are analyzed off-line (see below).

As detailed above in Sec. 8, the high voltage server program monitors the RICH HV status, by reading voltage and current values, and watching for trips. Also as detailed above, the RICH gas system and the cooling system adequately control critical operating parameters, but also provide for web-based monitors which are checked twice per hour during normal operation. For the gas system, the expansion volume transparency, the TEA bubbler temperature and the expansion volume oxygen content are closely monitored. For the cooling system, the chamber temperatures are watched. The operating parameters of the readout electronics is checked using the web-based utilities of the Slow Control system.

In addition, RICH performance is supervised offline, with a set of quality-monitoring plots produced from a prescaled sample of incoming events, from the so-called CLEO pass1 analysis. These are examined after each run, and include distributions of Cherenkov angles and photon yields from fast tracking, as well as the more pedestrian distributions of raw hits and cluster pulse heights (as described in Sec. 10).

This information has been sufficient to ensure that the CLEO RICH detector produced data with a high degree of stability over many years.

9.2 Chamber Gain Equalization

The high voltage operating point for all chambers was determined by a gain equalization procedure, which sought to make equal the pad-gain for single photons averaged over each window module individually. The gains were set to be below 25,000 in order to avoid discharges.

Gain changes were measured as a function of window and wire voltages. The gains were determined for each window-sized module by fitting an exponential curve to the pulse-height spectrum. We parameterized the gain as a function of the wire voltage, for each window voltage.

Gains of all of the chambers were varied by changing the voltages in an iterative manner in order to make them equal. Our goal was to have a pad-gain of ~23,000. Fig. 34 shows the distribution of gains as measured after the gains had been equalized. We find a mean of 23,400 with a fitted r.m.s. spread of 10%. Fig. 34 shows the distribution of gains as measured after the gains had been equalized. We find a mean of 23,400 with a fitted r.m.s. spread of 10%. This has remained stable during detector operation.
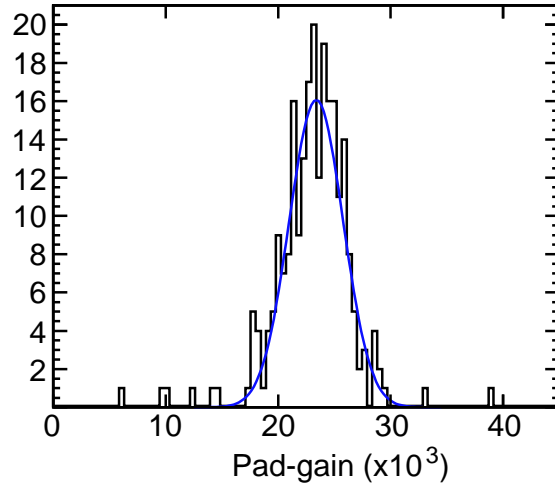
Fig. 34. Distribution of measured pad-gains, segmented for each window module separately.

9.3 Electronics Performance in CLEO III and CLEO-c

During data taking we routinely perform two sets of measurements to check the electronics performance. We measure the pedestal periodically, to verify that no baseline shifts occurred. These data also allow us to monitor the value of the total and incoherent noise of each channel. Typical noise distributions are shown in Fig. 35. The noise reduction produced by the coherent noise
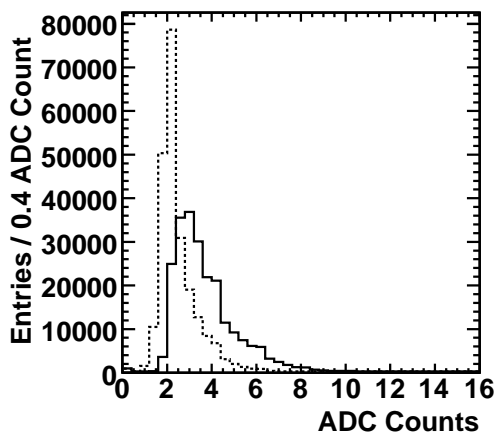
Fig. 35. Typical noise distributions for all channels in units of ADC channels (1 ADC channel equals ∼200 e⁻). The solid line shows the total noise while the dashed line shows the incoherent component after the coherent noise subtraction.

suppression can be clearly seen. The noise levels are quite low, the peak of the incoherent noise is at 425 electrons.
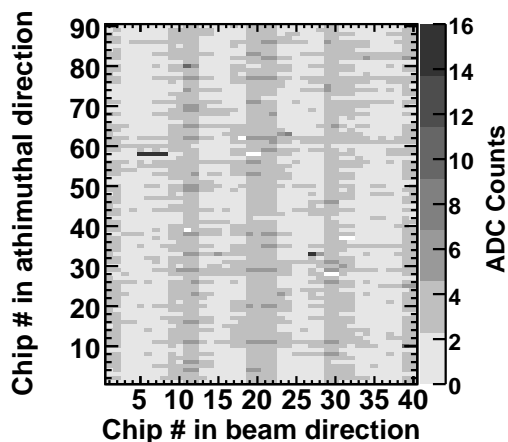

Fig. 36. Spatial distribution of the typical intrinsic noise on each VA_RICH chip, given in units of ADC counts. (The RICH cylinder is unfolded onto a plane.) There are slightly elevated noise bands at each end of a chain.

Fig. 36 shows a scatter plot of the intrinsic noise distribution across the detector. The horizontal axis corresponds to the length of the chambers and the vertical axis corresponds to the chamber number. It can be seen that the profile is rather uniform. The darker areas correspond to break points between different chamber sectors, and are associated with additional noise sources at the boundary between two adjacent sectors. Cross-talk or additional digital noise in the chip carrier at the end of a chain may cause this higher noise level.

The overall noise performance has been extremely stable throughout the years. Fig. 37 shows the time evolution of the mean value of the total noise and its
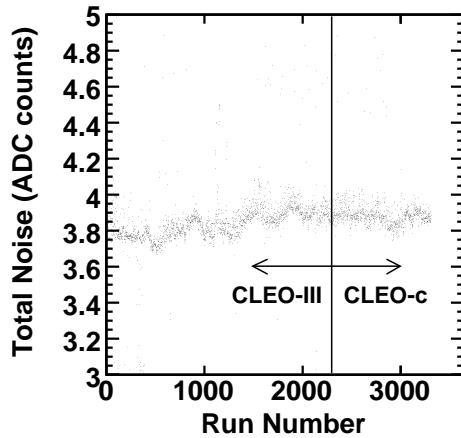
Fig. 37. Time evolution of the mean of the total noise. The time covered is about 5 years.

very stable value.
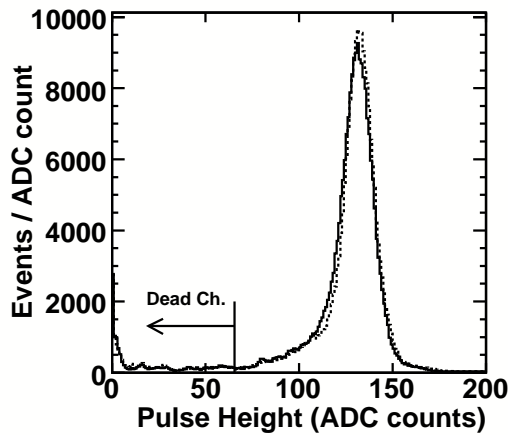
Fig. 38. Distribution of signals on all pads from injecting pulses on the wires of ± 5 mV. The solid line shows positive signals and the dashed line negative signals. Data is from the CLEO-c era.

An additional quantity that needs to be monitored is the gain of the front end electronics. In principle, we could undertake the same sort of electronics calibration that was performed to verify that the hybrids were compliant with all our specifications. However, the amount of data to be transferred is beyond the capabilities of the data acquisition system. Thus, we use a method that is much quicker and simpler, although not as accurate. We pulse the MWC wires and the capacitive coupling between wire and pad produces the current pulse amplified by the front end electronics. The advantage of this calibration procedure is that the current originates at the same location as the real signal. Thus it tests the integrity of the whole processing chain, including the wire bond between input channel and hybrid trace and all the connectors along the signal path. On the other hand, the pulse shape is not perfect because of

53

the improper termination, thus the gain measurement is not very accurate, as illustrated in Fig. 38, that shows the signal distribution on all the pads for input pulses of $+5$ mV and -5 mV respectively. The wire pulse distribution is also used to determine the number of dead channels. We have about 5% dead channels, and the number has been relatively stable throughout the duration of the experiment. These losses include one damaged multi-wire ribbon cable and ASIC damage as well as lost wirebonds.

The most notable source of ASIC loss has been occasional latch-up of these devices, due to the activation of parasitic PNPN paths in the device. The symptoms include large current draw and a different pedestal profile along the ASIC, much "flatter" than in a functioning ASIC. This phenomenon occurred more frequently in the early stages of the experiment, due to occasional faulty start-up procedures, that caused some device destruction. After we refined the start-up procedure, to prevent regenerative loops from occurring, the number of flat ASICs has remained stable, with some signs of recent recovery.

In general, we can say that the operation of this system has been very stable and reliable and no tuning of the bias voltages and currents has been necessary, since the initial adjustment performed upon installation.

10 DATA ANALYSIS AND PHYSICS PERFORMANCE

10.1 Introduction

The CLEO III detector was used for studies at the $\Upsilon(1S) - \Upsilon(5S)$ resonances from August of 2000 to March of 2003. The CLEO detector was then modified by replacing the silicon strip vertex detector with a low mass wire chamber. The magnetic field was also lowered from 1.5 T to 1.0 T, to help increase the machine luminosity. Data was then taken from October of 2003 until April of 2005. The results in this section refer to the first period as CLEO III and the second period as CLEO-c. More CLEO-c data will be forthcoming.

Coherent noise suppression and data sparsification are performed on-line to eliminate the Gaussian part of the electric noise. A small non-Gaussian component of the coherent electric noise is eliminated off-line, by using an algorithm too complicated for use in the data board DSP. The incoherent part of non-Gaussian noise was eliminated by off-line pulse height thresholds adjusted to keep occupancy of each channel below 1%. Finally, we eliminate clusters of cathode pad hits that are extended along the anode wires, but are only 1–2 pads wide in the other direction.
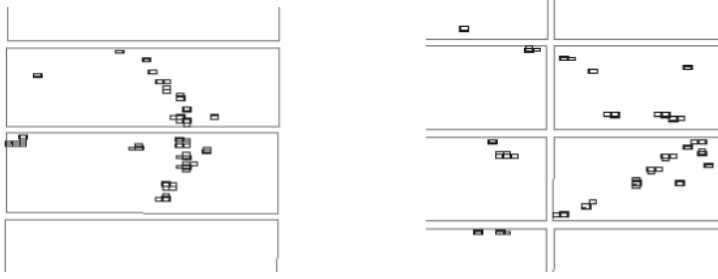
Fig. 39. Raw hit patterns produced by the particle passing through the plane (left) and sawtooth (right) radiators. Each rectangle indicates a pad channel above threshold.

We show in Fig. 39 the hit pattern in the detector for a Bhabha scattering event ($e^+e^- \rightarrow e^+e^-$) for track entering the plane (left image) and sawtooth (right image) radiators. The shapes of the Cherenkov "rings" are different in the two cases, resulting from refraction when leaving the LiF radiators. The hits in the centers of the images are produced by the electron passing the RICH multi-wire chambers.

10.2   Clustering of Hits

The entire detector contains 230,400 cathode pads, which are segmented into 240 modules of 24×40 pads separated by the mounting rails and anode wire spacers. We cluster pad hits in each module separately. Pad hits touching each other either by a side or a corner form a "connected region." Each charged track reconstructed in the CLEO tracking system [29] is projected into the RICH and matched to the closest connected region. If the matching distance between the track projection and the center of the connected region is reasonably small and the total pulse height of the connected region sufficiently high, we associate this group of hits with the track. Local pulse height maxima in the remaining connected regions, so-called "bumps," are taken as seeds for Cherenkov photons. We allow the pulse height maxima to touch each other by corners if the pulse height in the two neighboring pads is small relative to both bump heights. Hits adjacent to the bumps on the sides are assigned to them in order of decreasing bump pulse height.

To estimate the position of the photon conversion point we use the center-of-gravity method corrected for the bias towards the central pad. For many Cherenkov photons we are able to detect induced charge in only one pad. Since the pad dimensions are about 8×8 mm^2, the position resolution in this case is $8 \, \text{mm}/\sqrt{12} = 2.3 \, \text{mm}$. For charged track intersections, which induce significant charge in many pads, the position resolution is 0.76 mm. The position resolution for Cherenkov photons which generate multiple pad hits is somewhere in between these two values. In any case, the photon position error is not a

significant contribution to the Cherenkov angle resolution (see below).

10.3   Corrections to the Track Direction

The resolution of the CLEO tracking system is very good in the bending view (the magnetic field is solenoidal in CLEO) [29]. The track position and inclination angle along the beam axis is measured less precisely. The r.m.s. of the observed RICH hit residual is 1.7 mm. Since the RICH hit position resolution is 0.76 mm as measured by the residual in the perpendicular direction, the RICH can clearly help in pinning down the track trajectory. This, in turn, improves Cherenkov resolution, especially for the flat radiators for which we observe only half of the Cherenkov image and thus are quite sensitive to the tracking error. The improvement is as much as 50% in some parts of the detector.

10.4   Reconstruction of the Cherenkov Angle

Given the measured position of the Cherenkov photon conversion point in the RICH, the charged track direction and its intersection point with the LiF radiator, we calculate a Cherenkov angle for each photon-track combination (θ_γ). We use the formalism outlined by Ypsilantis and Séguinot [6], except that we adopt a numerical method to find the solution to the equation for the photon direction, instead of simplifying it to a fourth-order polynomial. The latter would allow an analytical solution, but at the expense of introducing an additional source of error. Furthermore, using our numerical method, we calculate derivatives of the Cherenkov angle with respect to the measured quantities which allows us to propagate the detector errors and the chromatic dispersion to obtain an expected Cherenkov photon resolution for each photon independently (σ_θ). This is useful since the Cherenkov angle resolution varies significantly even within one Cherenkov image. We use these estimated errors when calculating particle ID likelihoods and use them to weight each photon when measuring the average Cherenkov angle for a track.

10.5   Performance on Bhabha Events

We first view the physics performance on the simplest type of events, Bhabha events, and then subsequently in hadronic events. The distribution of Cherenkov angles measured for each photon in Bhabha events is shown in Fig. 40.

We note that Bhabha events have very low multiplicity compared with our nor-
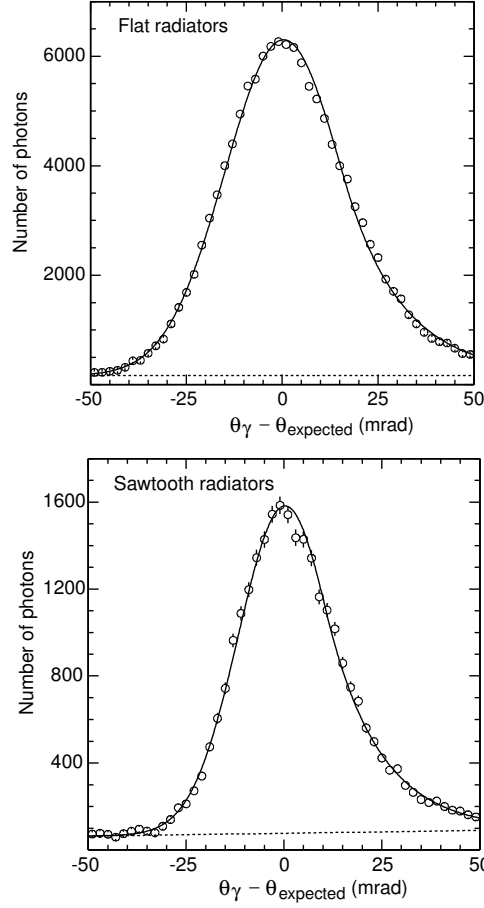
Fig. 40. The measured minus expected Cherenkov angle for each photon detected in Bhabha events, (top) for plane radiators and (bottom) for sawtooth radiators. The curves are fits to a special line shape function (see text), while the lines are fits to a background polynomial.

mal hadronic events. They have two charged tracks present while the hadronic events have an average charged multiplicity of approximately 10 in CLEO III. In addition, the hadronic events have on the average 10 photons, mainly from π^o decays. All of these particles can interact in the calorimeter and the splash-back can hit the RICH photon detector.

The Cherenkov angle spectrum for single photons has an asymmetric tail and modest background. It is fit with a line-shape similar to that used when extracting photon signals from electromagnetic calorimeters [30]. The functional form is

$$P(\theta|\theta_{exp}, \sigma_\theta, \alpha, n) = \tag{2}$$

$$A \cdot \exp\left[-\frac{1}{2}\left(\frac{\theta_{exp} - \theta}{\sigma_\theta}\right)^2\right] \text{ for } \theta < \theta_{exp} - \alpha \cdot \sigma_\theta$$

57
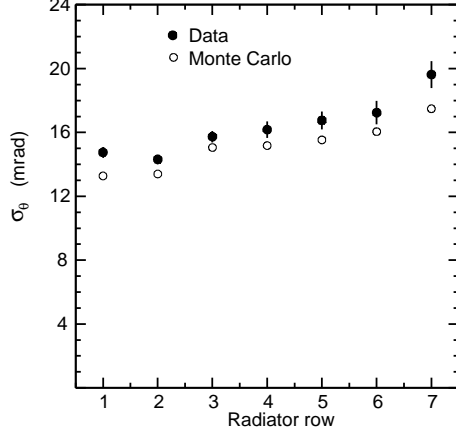
Fig. 41. The values of the Cherenkov angular resolution for single photons for data compared with Monte Carlo simulation as a function of radiator ring number. The four-rings of sawtooth radiators are in rings numbered 1 and 2, at the center of the detector.

$$A \cdot \frac{\left(\frac{n}{\alpha}\right)^n e^{-\frac{1}{2}\alpha^2}}{\left(\frac{\theta_{exp}-\theta}{\sigma_\theta} + \frac{n}{\alpha} - \alpha\right)^n} \qquad \text{for } \theta > \theta_{exp} - \alpha \cdot \sigma_\theta,$$

$$A^{-1} \equiv \sigma_\theta \left[\frac{n}{\alpha} \frac{1}{n-1} e^{-\frac{1}{2}\alpha^2} + \sqrt{\frac{\pi}{2}} \left(1 + \text{erf}\left(\frac{\alpha}{\sqrt{2}}\right) \right) \right].$$

Here θ is the measured angle, θ_{exp} is the "true" (or most likely) angle and σ_θ is the angular resolution. To use this formula, the parameter n is fixed to value of about 5.

The data in Fig. 40 are fit using this signal shape plus a polynomial background function. We compare the results of these fits for the resolution parameter σ_θ as a function of radiator ring [19] for data and Monte Carlo simulation in Fig. 41. Here we use the symmetry of the detector about the center to map two full physical radiator rings into a single ring number, with ring 1 being closest to the middle. The single photon resolution averaged over the detector solid angles are 14.7 mr for the flat radiator and 12.2 mr for the sawtooth.

The number of photons per track within $\pm 3\sigma$ of the expected Cherenkov angle for each photon is shown in Fig. 42 and shown as a function of radiator row in Fig. 43. Averaged over the detector, and subtracting the background, we have a mean number of 10.6 photons with the flat radiators and 11.9 using the sawtooth radiators.

The resolution per track is obtained by taking a slice within $\pm 3\sigma$ of the expected Cherenkov angle for each photon and forming an average weighted by $1/\sigma_\theta^2$. These track angles are shown in Fig. 44.

_____

[19] Effectively, this shows the dependence of the resolution on polar angle.
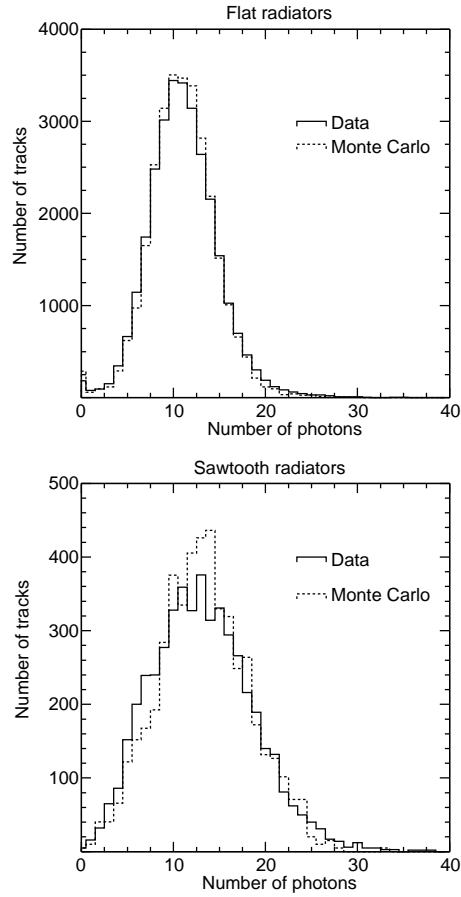
Fig. 42. The number of photons detected on Bhabha tracks (top) for plane radiators and (bottom) for sawtooth radiators. The dashed lines are predictions of the Monte Carlo simulation.
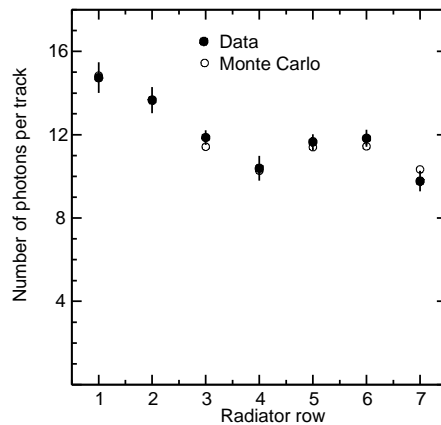

Fig. 43. The number of photons as a function of radiator row for Bhabha events. (Sawtooth radiators are in rings 1 and 2.)

The r.m.s. spreads of these distributions are identified as the track resolutions. We obtain 4.7 mr for the flat radiators and 3.6 mr for the sawtooth. The resolutions as a function of radiator row are shown in Fig. 45.
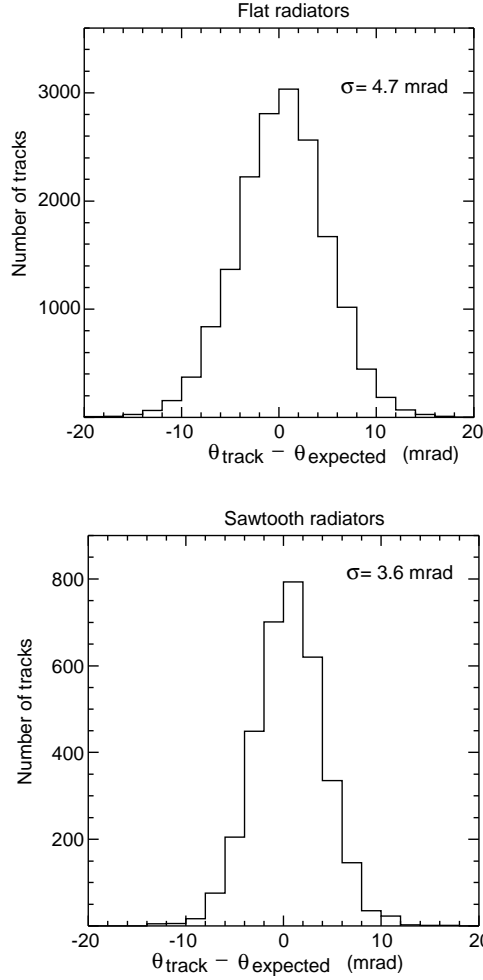
Fig. 44. Measured Cherenkov angle for each track in Bhabha events, (top) for plane radiators and (bottom) for sawtooth radiators.
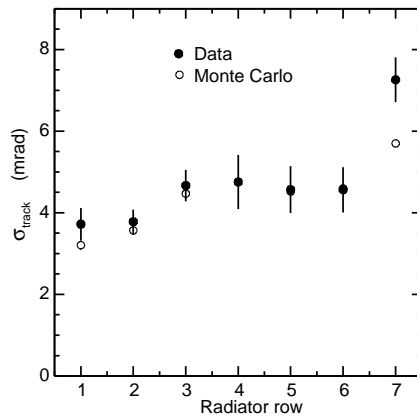
Fig. 45. Cherenkov angle resolutions per track as a function of radiator row for Bhabha events. (Sawtooth radiators are in rings 1 and 2.)

The Cherenkov angular resolution is comprised of several different components. These include: error on the location of the photon emission point, the chromatic dispersion, the position error in the reconstruction of the detected
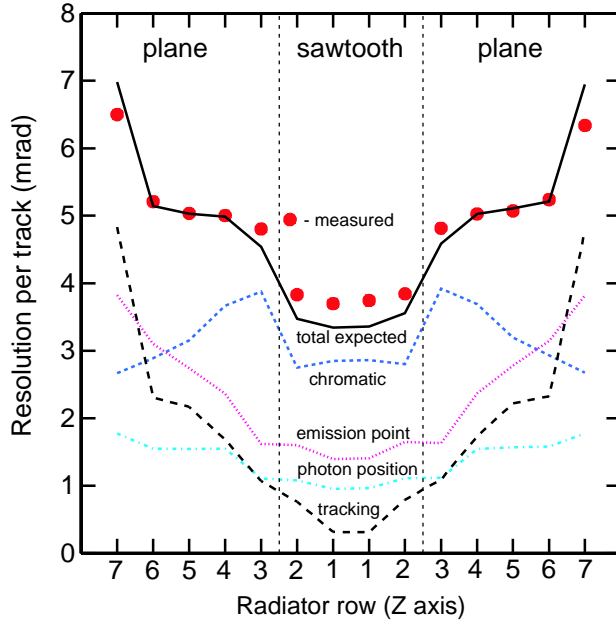
Fig. 46. Different components contributing to the Cherenkov angle resolution per track shown as a function of radiator row for Bhabha events. The points are data and the solid line is the sum of the predicted resolution from each of the individual components indicated on the figure.

photons, and finally the error on determining the charged track's direction and position. These components are compared with the data in Fig. 46.

10.6 Performance on Hadronic Events in CLEO III

To resolve overlaps between Cherenkov images for different tracks we find the most likely mass hypotheses. Photons that match the most hypothesis within $\pm 3\sigma$ are then removed from consideration for the other tracks. To study the RICH performance in hadronic events in CLEO III [20] we use $D^{*+} \to \pi^+ D^0$, $D^0 \to K^- \pi^+$ events. The charge of the slow pion in the D^{*+} decay is opposite to the kaon charge in subsequent D^0 decay. Therefore, the kaon and pion in the D^0 decay can be identified without use of the RICH detector. The effect of the small combinatorial background is eliminated by fitting the D^0 mass peak in the $K^- \pi^+$ mass distribution to obtain the number of signal events for each momentum bin. The $K^- \pi^+$ invariant mass distribution selected by requiring that the $K^- \pi^+ \pi^+$ - $K^- \pi^+$ mass difference be within 2.5 r.m.s. widths of the known mass difference is shown in Fig. 47. Here both the kaon and the pion are required to have momenta > 0.6 GeV/c.

Single-photon Cherenkov angle distributions obtained on such identified kaons with the momentum above 0.7 GeV/c are plotted in Fig. 48. Averaged over

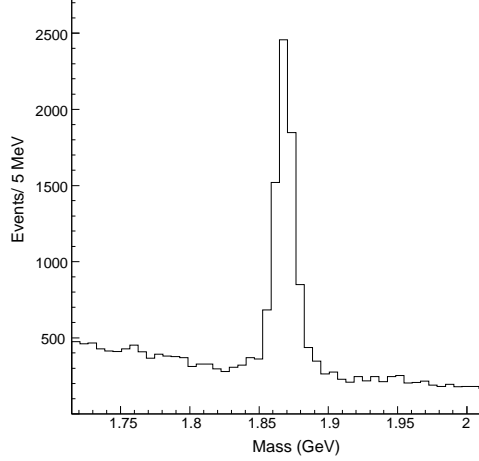[20] Until now CLEO-c has been running below threshold for the production of D^*'s.

Fig. 47. The $K^{\mp}\pi^{\pm}$ mass after selecting events with $K^{-}\pi^{+}\pi^{+}$ - $K^{-}\pi^{+}$ mass differences close to the known $D^{*}-D$ mass difference.

all radiators, the single-photon resolution is 13.2 mr and 15.1 mr for sawtooth and flat radiators respectively. The background fraction within $\pm 3\sigma$ of the expected value is 12.8% and 8.4%. The background-subtracted mean photon yield is 11.8 and 9.6. Finally the per-track Cherenkov angle resolution is 3.7 mr and 4.9 mr.

10.7 Particle ID Likelihoods

For parts of the Cherenkov image for the sawtooth radiator, and for tracks intersecting more than one radiator there are some optical path ambiguities that impact the Cherenkov angle calculations. In the previous section we bypassed this problem by selecting the optical path that produces the closest Cherenkov angle to the expected one (θ_{exp}^{h}) for the given particle hypothesis (h). There is some loss of information in this procedure, therefore, we use the likelihood method to perform particle identification instead of the per-track average angle. The likelihood method weights each possible optical path by the optical probability (P_{opt}), which includes length of the radiation path and the refraction probabilities obtained by the inverse ray tracing method:

$$
L_h = \prod_{j=1}^{No.\,of\,\gamma s} \left\{ P_{background} + \right.
$$

$$
\left. \sum_{opt} P_{opt}^{j} \cdot P_{signal}\left(\theta_{\gamma}^{opt,j} | \theta_{exp}^{h},\, \sigma_{\theta}^{opt,j}\right) \right\}
$$

where, L_h is the likelihood for the particle hypothesis h (e, μ, π, K or p), $P_{background}$ is the background probability approximated by a constant and
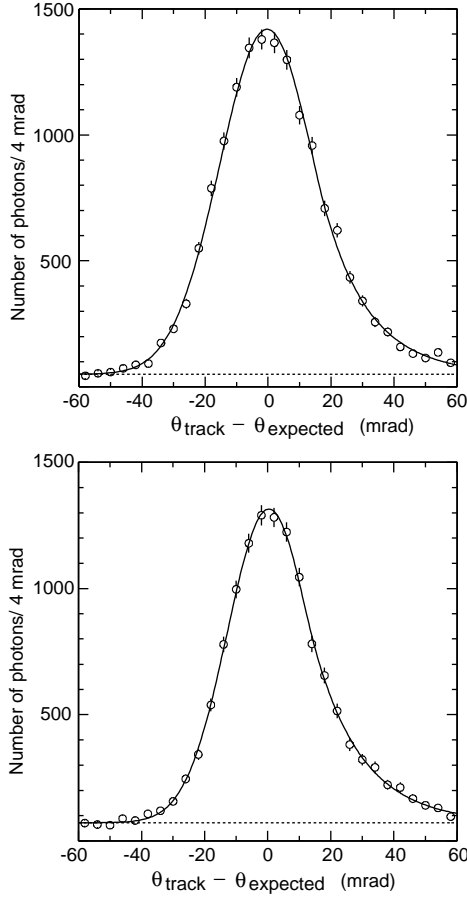
62

Fig. 48. The measured minus expected Cherenkov angle for each photon detected in hadronic events, (top) for plane radiators and (bottom) for sawtooth radiators. The curves are fits to special line shape function (see text), while the lines are fits to a background polynomial.

P_{signal} is the signal probability given by the line-shape defined previously. In principle, the likelihood could include all hits in the detector. In practice, there is no point in inspecting hits which are far away from the regions where photons are expected for at least one of the considered hypotheses (we use $\pm 5\sigma$ cut-off).

An arbitrary scale factor in the likelihood definition cancels when we consider likelihood ratios for two different hypotheses. The likelihood conveniently folds in information about values of the Cherenkov angles and the photon yield for each hypothesis. For well separated hypotheses (typically at lower momenta) the photon yield that provides some discrimination. Since our likelihood definition does not know about the radiation momentum threshold, the likelihood ratio method can be only used when both hypotheses are sufficiently above the thresholds. When one hypothesis is below the radiation threshold we use the value of the likelihood for the hypothesis above the threshold to perform the discrimination.
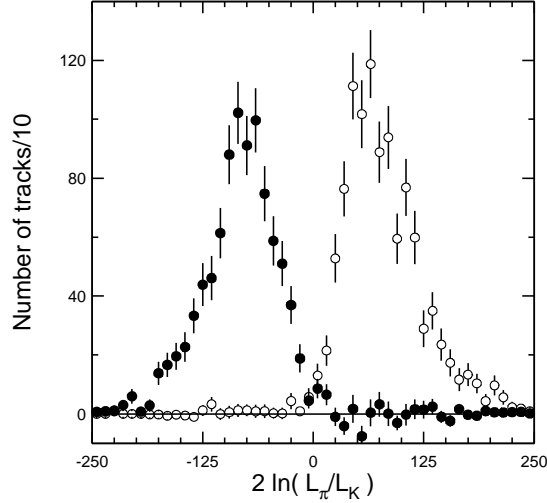
Fig. 49. Distribution of $2\ln(L_\pi/L_K) \sim \chi_K^2 - \chi_\pi^2$ for 1.0-1.5 GeV/c kaons (filled) and pions (open) identified with the D^* method.
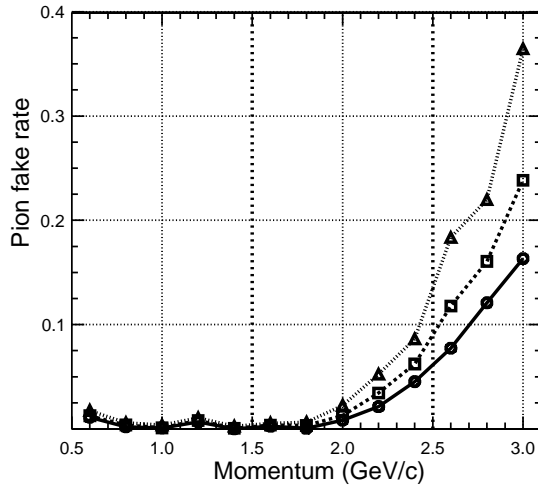

Fig. 50. Pion fake rate as a function of particle momentum for kaon efficiency of 80% (circles), 85% (squares) and 90% (triangles).

The distribution of the $2\ln(L_\pi/L_K)$, is expected to behave as the difference $\chi_K^2 - \chi_\pi^2$. This χ^2 difference obtained for 1.0-1.5 GeV/c kaons and pions identified with the D^* method is plotted in Fig. 49. Cuts at different values of this variable produce identification with different efficiency and fake rate. Pion fake rates for different values of kaon identification efficiency are plotted as a function of particle momentum in Fig. 50. Here when the fake rates get below a few percent there are other systematic effects that enter. For example, doubly Cabibbo suppressed decays where the D^o decays into a $K^+\pi^-$ rather than a $K^-\pi^+$ have a relative branching fraction of 0.4% [33].

64

Here we use 180 pb^{-1} integrated luminosity of CLEO-c data produced in e^+e^- collisions and recorded at the ψ'' resonance (3.770 GeV). At this energy, the events consist of a mixture of pure D^+D^-, $D^o\overline{D}^o$, three-flavor continuum event and $\gamma\psi'$ events. There may also be small amounts of $\tau^+\tau^-$ pairs and two-photon events.

In this study we select events containing at least one neutral D candidate in the following decays $D^o \rightarrow K^-\pi^-\pi^+\pi^+$, $D^o \rightarrow K^-\pi^+$ and $D^o \rightarrow K^-\pi^+\pi^o$. (Charge conjugate modes are also used.) Event candidates in these modes are mostly signal with low background fractions. The D^o candidate invariant mass plots are shown in Fig. 51. These mass plots are constructed by selecting decays where the sum of the measured energies is close to the electron beam energy and then using the measured beam energy to form the mass [34]. We use this sample to look for two oppositely charged tracks present in the other side of the event not containing the tagged D. We then further select events where the $\overline{D}^o$ decays into $K^\pm\pi^\mp$. The momentum spectra of the kaon and the pion from this decay when the D is produced on the $\psi(3770)$ is shown in Fig. 52.

We start by describing the analysis of the joint decays $\overline{D}^o \rightarrow K^+\pi^-\pi^+\pi^-$ and $D^o \rightarrow K^\pm\pi^\mp$. Here we define the decay into $K^-\pi^+$ as "right" sign and the decay into $K^+\pi^-$ as "wrong" sign. In this case the wrong sign decays could result from one of three sources: background, doubly Cabibbo suppressed decays or $D^o-\overline{D}^o$ mixing. We note that current measures of mixing limit it to $\sim<0.045\%$ [35], while current measures of doubly Cabibbo suppressed decays are larger. For example, the modes $K^-\pi^+$, $K^-\pi^-\pi^+\pi^+$ and $K^-\pi^+\pi^o$ have rates of 0.35%, 0.42%, and 0.43%, respectively.

Fully reconstructed single tags for the $K^+\pi^-\pi^+\pi^-$ mode (and its charge conjugate, which will not be explicitly mentioned in what follows) are reconstructed using the beam constrained mass. We use a 2σ cut on ΔE and require the mass to be between 1.86 and 1.870 GeV. We then form a double tag event using either right or wrong sign $K\pi$ decays. We use a tight cut on the $K\pi$ of $|\Delta E|$, the difference between the measured energy and the beam energy within 2σ, where σ is the r.m.s. of the distribution. Since we need to use the RICH we impose a cut that both tracks be within $|\cos(\theta)| < 0.81$, where θ is the angle of the track with respect to the beam line.

At first we do not use any RICH identification on the $K\pi$. Using a total of 180 pb^{-1} we have 1158 such events where the kaon and pion are both in the RICH acceptance that give the right sign and the same sample yields 642 wrong sign events.
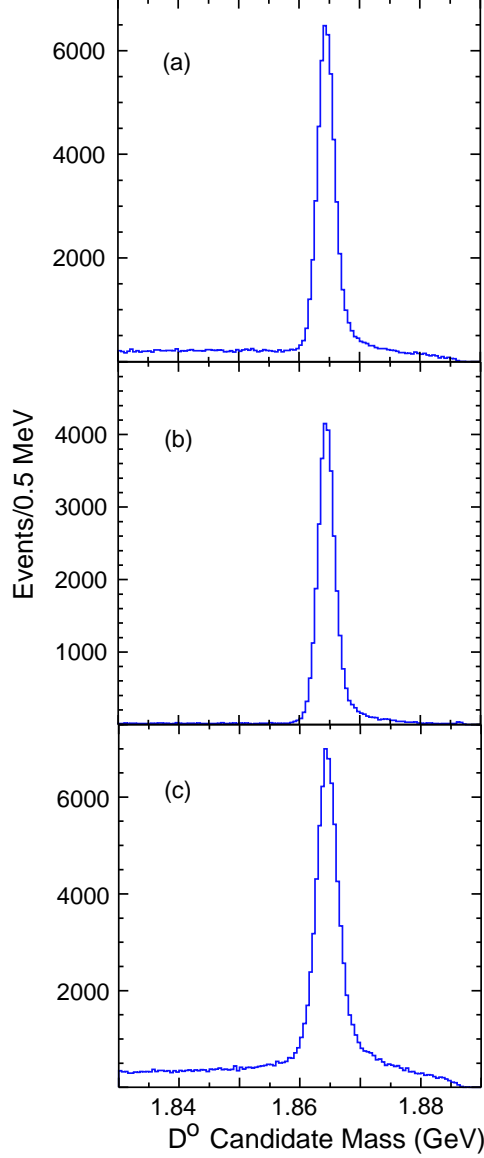
Fig. 51. Beam constrained mass distributions for (a)$K^-\pi^-\pi^+\pi^+$, (b) $K^-\pi^+$, and (c) $K^-\pi^+\pi^o$ candidates.

We now make three separate analyses: one where we identify only the kaon, one where we identify only the pion and one where we identify both the kaon and the pion. In the latter case we insist that there is significant discrimination in both cases or we do not accept the event.

Since the fake rates will be near 2%, the probability of getting both the kaon and the pion wrong is $\sim 4 \times 10^{-4}$, so that asking for a double identification is sufficient to ensure that we are getting the right answer for this level of tags.

The results are shown in Table 2. We find 1158 right sign events without using any particle identification, 970 right sign events with both particles identified, 15 wrong sign events with both particles identified, 25 events with
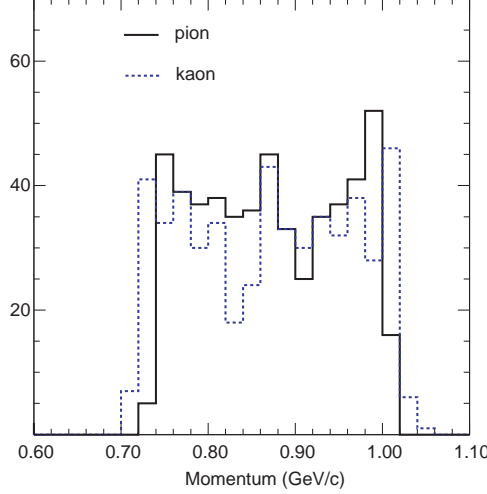
Fig. 52. The kaon and pion momentum spectra from $D \to K^{\pm}\pi^{\mp}$ decays.

only the kaon identified incorrectly and 36 events with only the pion identified incorrectly.

Mode	No ID		Single K		Single π		Double ID	
	(RS)	(WS)	(RS)	(WS)	(RS)	(WS)	(RS)	(WS)
$K^-\pi^-\pi^+\pi^+$; $K^{\pm}\pi^{\mp}$	1158	642	1021	25	105	36	970	15
$K^-\pi^+$; $K^{\pm}\pi^{\mp}$	307	199	273	3	295	6	264	0
$K^-\pi^+\pi^o$; $K^{\pm}\pi^{\mp}$	1524	897	1350	14	1444	22	1287	4
Sum	2989	1738	2644	42	2842	64	2521	19

Table 2

Results of RICH identification on double tag events. RS indicates right sign and WS indicates wrong sign events.

The 15 doubly identified wrong sign events are the combination of background, doubly Cabibbo suppressed decays and mixing. They correspond to a rate of these events of $(1.5\pm0.4)\%$, consistent with them all being doubly Cabibbo suppressed decays, but somewhat larger [33]. We subtract these events after correcting for the efficiency for the wrong sign candidates. This gives us a kaon fake rate of 1.1%, with an efficiency for events in the RICH of 88.5% and a pion fake rate of 3.7%, with an efficiency of 93.7%. We note that background is likely to be absent or small in these double tag events, but need to make a quantitative assessment.

To ascertain the background level we plot the beam constrained mass of the $K^-\pi^+\pi^+\pi^-$ tag versus the $K^{\pm}\pi^{\mp}$ tag in Fig. 53. Events outside of the region where both masses are greater than 1.858 GeV are background. There is only one background event in the wrong sign plot indicating that the background is much less than one event.
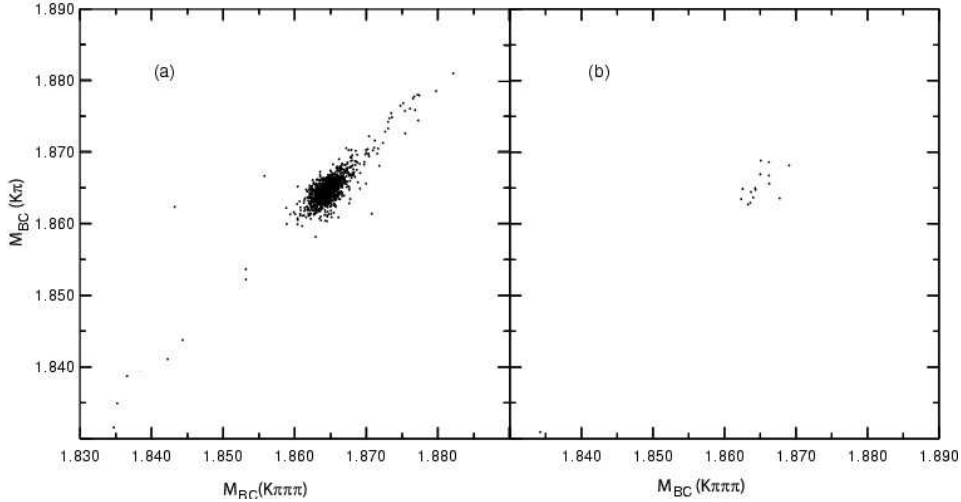
Fig. 53. Beam constrained mass for $K^-\pi^-\pi^+\pi^+$ versus $K^\pm\pi^\mp$; (a) Right sign events, (b) wrong sign events.

We now consider the case where both neutral D's decay into $K^\pm\pi^\mp$. One difference in this case with other cases is that doubly Cabbibo decays are forbidden due to Bose-Einstein statistics [36]. The results are presented in Table 2. Here there is wrong sign doubly identified decay. This could be due to (a) background (b) D^o mixing or (c) where both particles were incorrectly identified. We find zero events in the wrong sign doubly identified decay. We plot the beam constrained mass of the $K^-\pi^+$ tag versus the $K^\pm\pi^\mp$ tag in Fig. 54.

Our final mode uses $K^-\pi^+\pi^o$ for the single tag. The results are also presented in Table 2. To ascertain the background level we plot the beam constrained mass of the $K^-\pi^+\pi^o$ tag versus the $K^\pm\pi^\mp$ tag in Fig. 55. Although there appears to be some background in the right sign plot, the wrong sign shows no evidence of background.

The 4 doubly identified wrong sign events are the combination of background, doubly Cabbibo suppressed decays and mixing. They correspond to a rate of these events of $(0.3\pm0.2)\%$, consistent with them all being doubly Cabibo suppressed decays, but somewhat smaller.

Using all three of these mode combinations we find the rate of pions faking kaons of $(1.10\pm0.37)\%$, with a pion efficiency for events in the RICH of $(94.5\pm0.4)\%$. The rate of kaons faking pions is (2.47 ± 0.38) %, with a kaon efficiency for events in the RICH of $(88.4\pm0.6)\%$. The lower kaon efficiency arises because a significantly larger fraction of kaons than pions decay in this momentum region. It should be emphasized that these values are obtained for the entire running period between October, 2003 and February of 2005, and includes all possible system effects.
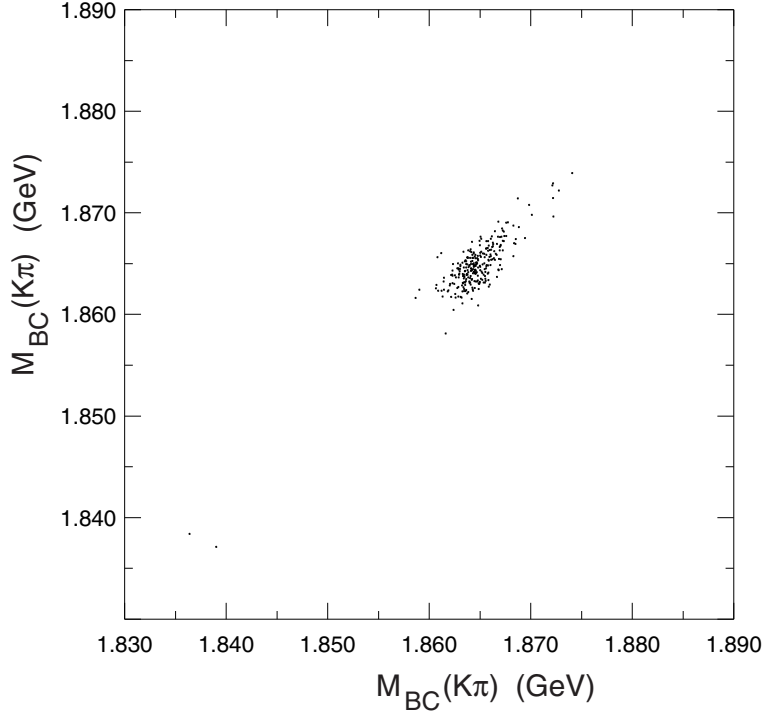
68

Fig. 54. Beam constrained mass for $K^-\pi^+$ versus $K^\pm\pi^\mp$.
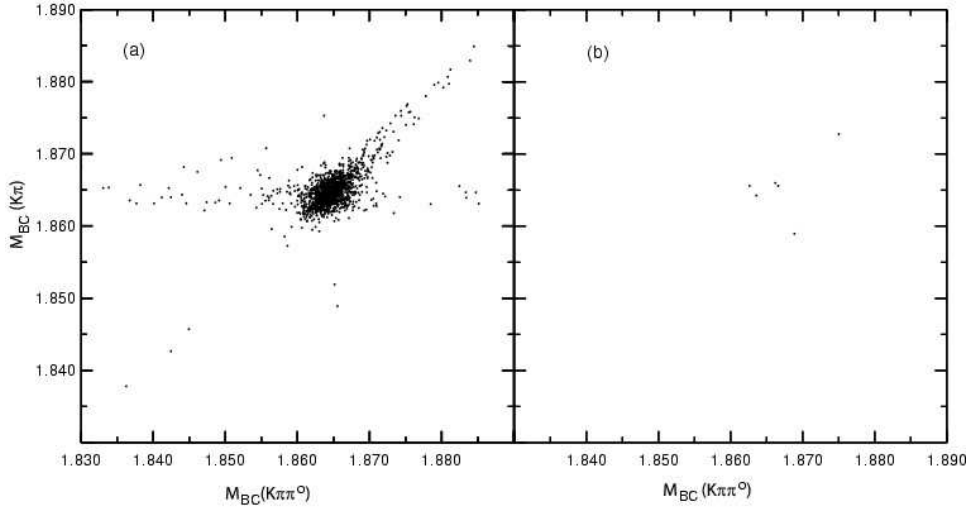

Fig. 55. Beam constrained mass for $K^-\pi^+\pi^o$ versus $K^\pm\pi^\mp$.

11 CONCLUSIONS

We have successfully constructed and operated a large, complex RICH detector in a particle physics experiment for over five years. The oxygen level has been kept below a few ppm in the "expansion volume" and the TEA photon conversion gas has been kept out, allowing for the Cherenkov photon yield to remain almost constant over the running period. We have lost some photon yield with a small ~5% failure of electronics chips. One broken wire has caused

an additional 1.7% loss and does somewhat effect the track efficiency. The total "cylindrical" detector thickness measured perpendicular to the axis is 13% of a radiation length.

The RICH is used during the normal course of most physics analyses using a standard set of criteria based on the minimum number of observed Cherenkov photons, usually 3, and the relative liklihood that a track is given type, either pion or kaon, for example.

The particle momenta for B meson decay products seen by CLEO III are less than 2.65 GeV/c. The detector provides excellent separation between pions and kaons at and below this cutoff. Separation between kaons and protons extends to even higher momentum, where it is used in charm studies. Thus, the physics performance has met design criteria. The RICH has provided crucially important particle separation in a number of important physics analyses including measurements of charmless hadronic two-body B meson decays and the ratio $\Gamma(B \to DK)/\Gamma(B \to D\pi)$ [37], and measurement of the form-factors in $D^o \to \pi^- \ell^+ \nu$ and $D^o \to K^- \ell^+ \nu$ decays [38].

CLEO is currently making an extensive study charm mesons and charmonium decays (called CLEO-c [32]). For these measurements the beam energy is lowered and the maximum particle momenta is about $1.0 - 1.5$ GeV/c. At these momentum the particle identification fake rates are at the 1% level.

12   ACKNOWLEDGEMENTS

Appendix A. VUV SPECTROPHOTOMETERS

The CH_4-TEA photosensitive gas inside the RICH chambers has an appreciable photo-absorption cross-section in a narrow VUV band $\lambda = 150 \pm 15$ nm. Satisfactory reconstruction of the Cherenkov cone geometry requires that the windows and the radiator crystals (especially their top surface), be sufficiently transparent in this wavelength band. A crystal surface which is poorly polished or contaminated would reduce significantly the number of photons emitted from the radiator crystals and subsequently degrade the Cherenkov angle measurement resolution.

Three VUV spectrophotometers used to measure the transmission of the crystals were built and placed at the three locations associated with crystal production and handling.

A.1. LiF VUV Transmission Spectrophotometer at SMU

Prior to installation of individual crystals onto the RICH Inner Cylinder, each crystal's transparency was measured using a specially constructed VUV spectrophotometer at four wavelengths: $\lambda = 135, 142.5, 150$ and 165 nm. The essential components of this transmission spectrophotometer are shown in Fig. 56. A vacuum monochromator with a deuterium lamp is the VUV light source. A test box 250 liter vacuum vessel contains the crystal to be measured, along with a two-dimensional stage driven by stepper motors. The crystal's top surface is held perpendicular to the direction of the probe radiation and collimators produce a beam spot of radius ~1 mm on the crystal surface. The stage can reliably position a crystal inside the vessel with a spatial precision of better than $25\,\mu$m along each of the stage's mutually perpendicular axes. It moves the crystal perpendicular to the beam direction in a raster style and periodically stops at discrete points while the transparency measurement is made. The typical spacing between measurements points is 1 cm. For calibration purposes, during each motion along the width of the crystal, the stage both moves the crystal completely out of the beam and completely blocks the beam with its frame, so as to provide measurements along each row of the scan that correspond to 100% and 0% transparency, respectively.

Both, the monochromator and the vacuum vessel, are evacuated by dedicated turbomolecular vacuum pumps to minimize absorption of the probe radiation by any residual air or water molecules. A photomultiplier tube (PMT), whose front window is coated with an ultraviolet wave-shifting compound (sodium salicylate [39]), is attached to the vacuum vessel and measures the intensity of the transmitted VUV light from the monochromator after its passage through
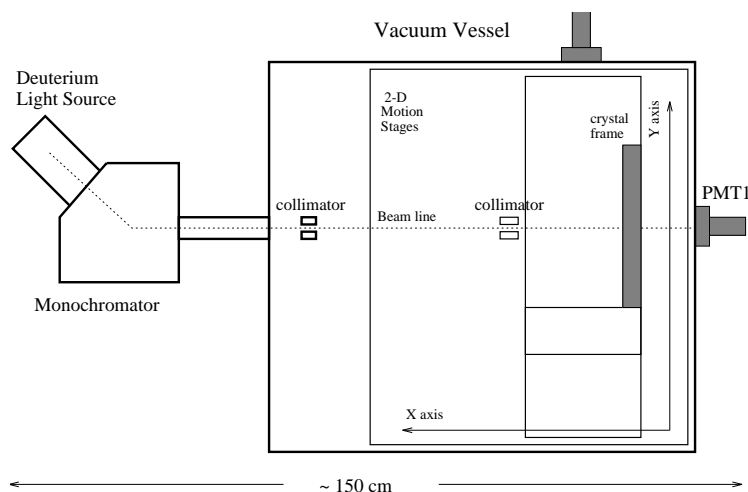
Fig. 56. Transmission measurement setup for the LiF planar radiator crystals.

the crystal. PMT output signals are amplified, filtered, digitized and then processed by a LabVIEW-based program to determine the crystal transparency map in real time. Data is also written to disk for further off-line analysis.

The measurement process was necessarily highly automatic and the control software ran on a PC, which in turn communicated with the data acquisition system and the stage controllers. The software controlled the high voltage for the PMT, monitored pressures in the two vacuum systems (monochromator and test box), and through a standard GPIB interface adjusted the monochromator grating to the desired wavelength. A graphical user interface allowed the user to set efficiently a wide range of control parameters to measure radiator crystals in a variety of modes, to measure crystal ingot test bars, and to perform calibration runs of various types.

Extensive adjustment and calibration of the spectrophotometer system were performed to minimize systematic errors and to measure overall system time stability and reproducibility. For example, the linearity of the electronic readout chain was measured to be much better than 1% over the range of readout voltages and transmission measurements separated in time by more than 1 month of the same LiF sample show agreement within 1%. Overall, $\simeq 500,000$ individual LiF transmission measurements were made.

A.2. VUV Spectrophotometer at Syracuse

A second VUV spectrophotometer similar in design was constructed at Syracuse University for the purpose of testing the window crystals as well as the sawtooth radiators.

The window crystals were measured in a manner substantially similar to that

described above for the planar radiators. Transmissions were measured at three wavelengths (135 nm, 150 nm, and 165 nm), and over a grid of 30 positions over the surface of the crystal window. For half-sized windows, there were 15 positions per crystal. The results are summarized in Section 3.2.

In this spectrophotometer, however, systematic uncertainties in the transmission measurements were reduced using different techniques. Before the light beam enters the vacuum tank, it is passed through a chopper which opens and closes at ~40 Hz. The resulting phototube current appears to be a square wave, with an amplitude that provides a measure of the light output, while automatically subtracting stray light and dark current offsets. Also, in general, the transmission measurement is made by performing "crystal-in/crystal-out" measurements: we divide the light output when the beam passes through a crystal (as registered by the current in the phototube) by the light output when the crystal is removed from the beam. Measuring this ratio attempts to divide out drifts in the lamp output or gain variations in the PMT over time. Making this reference measurement frequently means that the measurement cannot drift appreciably from point-to-point within a scan. Individual transmission measurements have a "statistical" uncertainty of typically 0.5–1.0% due to averaging the photocurrent, and a 0.5–1.0% "systematic" uncertainty due to signal drift over a typical measurement interval.
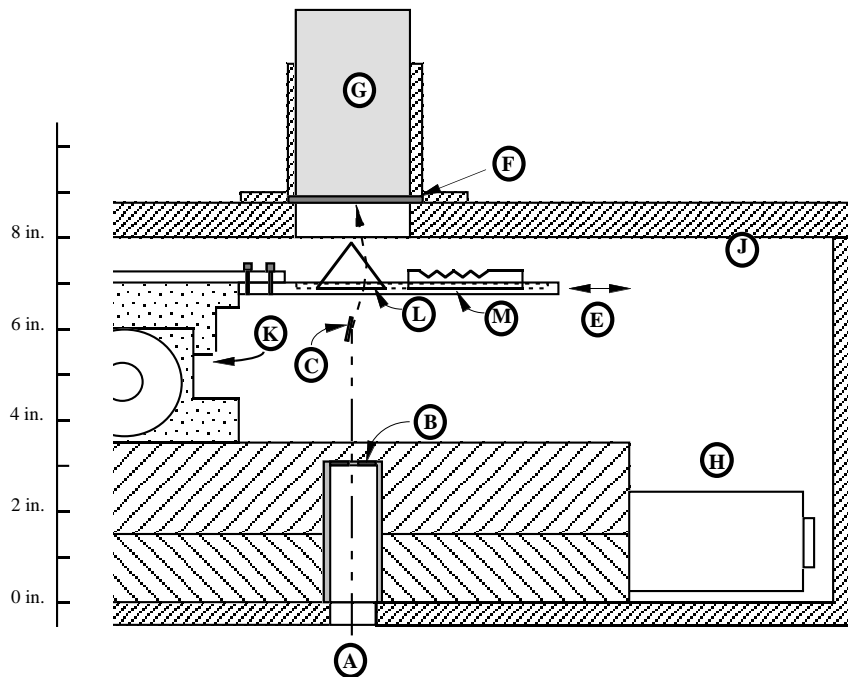

Fig. 57. Transmission measurement setup for the LiF sawtooth radiator crystals. Components are: (A) monochromator light beam, (B) collimating slit, (C) VUV mirror, (E) crystal holder tray mounted on X-Y stage, (F) sodium salicylate covered glass window, (G) Photomultiplier tube, (H,K) X,Y-axis linear stage, (J) vacuum tank wall, (L) 42° VUV-polished prism, and (M) sawtooth radiator. (Only four grooves of the sawtooth radiator are shown, for illustrative purpose.

The sawtooth radiators required a special technique in order to measure their transmission. For this, the spectrophotometer is configured as shown in Fig. 57. The monochromator light beam enters through the bottom of the vacuum tank, and passes through a 0.020 inch collimating slit. The pencil beam has a Gaussian shape with $\sigma = 25$ μm. The light reflects off of an adjustable mirror to produce a 15° deflection of the beam. It passes through a 42° VUV-polished prism, which is mounted on the two-dimensional stage. The light is wavelength-shifted by the sodium salicylate covered glass window, and detected in the photomultiplier tube.

The angular deflection of 15° is set so as to probe the transmission at the smallest possible angle that is not totally internally reflected and that accrues appreciable signal. Although the Fresnel coefficients are functions of incident angle at an interface, the important point is that the prism has the same shape as the sawtooth radiator grooves. Hence, by moving the stage such that the prism and sawtooth crystal passes through the beam, a relative transmission measurement using the prism as a standard may be made. Uncertainties were at the 1% level.

A third spectrophotometer, a duplicate to this system, was constructed and placed on site at the crystal manufacturing company in order to make quality assurance measurements of the window and planar radiator crystals before shipping.

References

[1] Y. Kubota et al., Nucl. Instr. Meth. A 320 (1992) 66.

[2] M. Artuso, "Progress Towards CLEO," in the Proceedings of the XXIX International Conference on High Energy Physics, Vancouver, Ed. by A. Astbury et al., World Scientific, Singapore, Vol. 2, p.1552, [hep-ex/9811031] (1998).

[3] S.E. Kopp, Nucl. Instr. Meth. A 384 (1996) 61.

[4] J. Séguinot and T. Ypsilantis, Nucl. Instr. Meth. A 343 (1994) 1.

[5] A similar system was tested previously, see R. Arnold et al., Nucl. Instr. Meth. A 314 (1992) 465; J.-L. Guyonnet et al., Nucl. Instr. Meth. A 343 (1994) 178; J. Séguinot et al., Nucl. Instr. Meth. A 350 (1994) 430.

[6] T. Ypsilantis and J. Séguinot, Nucl. Instr. Meth. A 343 (1994) 30.

[7] J. Séguinot, Les Compteurs Cherenkov, Lectures given at L'Ecole Joliot-Curie, Maubuisson, France, 1988 (Les Editions de Physique, 1989).

[8] M. Artuso et al., Nucl. Instr. Meth. A 441 (2000) 374 [hep-ex/9910054].

[9]   M. Artuso et al., Nucl. Instr. Meth. A 461 (2001) 545 [hep-ex/0008007].

[10] A. Efimov and S. Stone, Nucl. Instr. Meth. A 371 (1996) 79.

[11] R. Bouclier et al., Nucl. Instr. Meth. A 205 (1983) 205.

[12] STADCO, Inc., Los Angeles, CA, 90031, `www.stadco.com`.

[13] IDEAS ASA, 1330 Fornebu, Norway, `www.ideas.no`.

[14] Optovac, Inc., North Brookfield, MA 01535 (Now a part of Corning, Inc., Corning, NY 14831.)

[15] D.C. Stockbarger, Rev. Sci. Instr. 7 (1936) 133.

[16] F. Twyman, Prism And Lens Making, Hilger & Watts, London, 1957.

[17] J.V.R. Kaufman and C.D. Clark, J. Chem. Phys. 38 (1963) 1388.

[18] P. Gorlich, H. Karras, and R. Lehmann, Phys. Stat. Sol. 1 (1961) 389.

[19] R.T. Williams, , M.N. Kabler, , W. Hayes, , and J.P. Stott, Phys. Rev. B14 (1976) 725.

[20] P. Gorlich, H. Karras, and G. Kotitz, Phys. Stat. Sol. 3 (1963) 1629.

[21] S. Timm et al., "TEA Aging Studies," CLEO Internal Note CBX 96-30 (1996)

[22] W.A. Campbell and J.J. Scialdone, Outgassing Data for Selecting Spacecraft Materials, NASA RP-1124, Rev.2, 1990; data is available online at outgassing.nasa.gov. Quantities quoted are Total Mass Loss (%TML) and Collected Volatile Condensable Materials (%CVCM).

[23] Composite Optics, Inc. (formerly R-Cubed Composites, Inc), San Diego, CA 92121, `www.coi-world.com`.

[24] PSL Engineering and Instrumentation, Stoughton, WI 53589, `www.psl.wisc.edu`.

[25] E. Nygard et al., Nucl. Instr. Meth. A 301 (1991) 506.

[26] LabVIEW, National Instruments, Inc., Austin TX, `www.ni.com`.

[27] LeCroy Corporation, Chestnut Ridge, NY 10977; now sold by Universal Voltronics Corporation, Brookfield, CT 06804, `www.voltronics.com`.

[28] A. Warburton et al., Nucl. Instr. Meth. A 488 (2002) 451.

[29] D. Peterson et al., Nucl. Instr. Meth. A 478 (2002) 142.

[30] T. Skwarnicki, "A Study of the Radiative Cascade Transitions Between the Upsilon-Prime and Upsilon Resonances," DESY F31-86-02 (thesis, unpublished) (1986).

[31] M. Artuso et al., Nucl. Instr. Meth. A 502 (2003) 91 [hep-ex/0209009].

[32] D. Asner, "The CLEO-c Research Program," in 9th Int. Conf. on B Physics at Hadron Machines (Beauty2003), Pittsburgh, PA, Oct., 2003, p82, ed. Paulini and Erhan, AIP, Melville, NY 2004.

[33] S. Eidelman et al. (PDG), Phys. Lett. B **592**, 1 (2004).

[34] Q. He et al. (CLEO), "Measurement of Absolute Hadronic Branching Fractions of D Mesons and $e^+e^- \rightarrow D\bar{D}$ Cross Sections at $E_{cm} = 3773$ MeV," [hep-ex/0504003].

[35] K. Abe et al. (Belle), Phys. Rev. Lett. **94** (2005) 071801. [hep-ex/0408125].

[36] I. I. Bigi and A. I. Sanda, "CP Violation," Cambridge Univ. Press, Cambridge, U. K. (2000), see problem 10.4, page 177.

[37] A. Bornheim et al. (CLEO) Phys. Rev. **D68** (2003) 052002 [hep-ex/0302026].

[38] G. S. Huang et al. (CLEO) Phys. Rev. Lett. **94** (2005) 011802 [hep-ex/0407035].

[39] J.A.R. Samson, Techniques of Vacuum Ultraviolet Spectroscopy, Pied Publications, Lincoln NE, 1967.